

Dilepton production at next-to-leading order and intermediate invariant-mass observables

Jessica Churchill,¹ Lipei Du,¹ Charles Gale,¹ Greg Jackson,^{2,3} and Sangyong Jeon¹

¹*Department of Physics, McGill University, 3600 University Street, Montreal, QC, Canada H3A 2T8*

²*Institute for Nuclear Theory, Box 351550, University of Washington, Seattle, WA 98195-1550, United States*

³*SUBATECH, Nantes Université, IMT Atlantique, IN2P3/CNRS,*

4 rue Alfred Kastler, La Chantrerie BP 20722, 44307 Nantes, France

(Dated: May 8, 2024)

The thermal QCD dilepton production rate is calculated at next-to-leading order in the strong coupling and at finite baryon chemical potential. The two-loop virtual photon self-energy is evaluated using finite temperature field theory and combined consistently with the self-energy in the Landau-Pomeranchuk-Migdal regime. We present new results for a dense baryonic plasma. The rates are then integrated using (3+1)-dimensional fluid-dynamical simulations calibrated to reproduce hadronic experimental results obtained at RHIC at energies ranging from those of the Beam Energy Scan to $\sqrt{s_{\text{NN}}} = 200$ GeV. We elaborate on the ability of dileptons to relay information about the plasma baryonic content and temperature.

I. INTRODUCTION

Heavy-ion collisions make it possible to study the strong nuclear force at temperatures and densities where the quark-gluon plasma (QGP) can exist [1]. Photons produced within the plasma are unobscured by the rest of the medium, making them (conceptually) ideal probes [2–6]. Those include both real and virtual photons; the latter of which decay into on-shell lepton-antilepton pairs. The electromagnetic radiation can originate from *all* stages of the nucleus-nucleus interaction, e. g. reactions involving initial (hard) partons would populate the high energy part of the spectrum and hadron decays (mostly π^0 's) would dominate the lower energy regions. Thus, a detailed understanding of specific production rates—particularly from the QGP itself—is a prerequisite to explaining the observations in general [7], and to turning electromagnetic radiation into useful calibrated probes of the strongly interacting medium.

Although dileptons are typically rarer than photons—their emission is suppressed by one power of α_{em} compared to that of real photons—they have an additional degree of freedom: the (non-zero) invariant mass, M . This extra parameter is important in enabling dileptons as a tomographic tool of the medium created in heavy ion collisions. In this capacity, lepton pairs are a good probe of the local temperature, as the differential lepton pair emission rate depends on the invariant mass, M , which is independent of the local fluid flow [8]. This is not the case for real photons¹ [10], but that dependence on the fluid flow can be exploited to inform the dynamical modeling of the collision [11]. In the context of heavy-ion phenomenology, measurements of real and virtual photons are therefore complementary.

Concerning thermal dilepton production,² as the sys-

tem evolves, QGP sources will compete with those associated with reactions involving composite hadrons such as mesons and baryons [19, 20]. The partonic reaction rates—relevant at high temperature—and the hadronic reaction rates—important at lower temperature—are integrated using approaches simulating the time evolution of the entire strongly interacting system. Some of the early phenomenological studies were based on parton cascades [21] and quasiparticle models [22], on a background of ideal hydrodynamics with radial symmetry [23], and on thermal fireballs [24]. Currently, (3+1)-dimensional viscous hydrodynamics studies are standard tools for analyses and interpretation of heavy-ion collision results, and dileptons have also been shown to be sensitive to viscosities (shear and bulk) and to details of the initial conditions [25–27].

Recently, a great deal of attention has been devoted to the baryon-dense region of the QCD phase diagram [28], which is being explored by the Beam Energy Scan (BES) program at RHIC, and by the NA61/SHINE experiment at the CERN SPS. The future NA60+ experiment is being proposed to measure the dimuon spectrum for baryon-rich systems [29, 30]. Anticipating detailed comparisons with those and other experiments, we concentrate solely on the thermal contribution from deconfined quarks and gluons, reporting on two aspects of this investigation: *i*) we generalize the NLO perturbative calculation of dilepton emission rates to non-zero baryon chemical potential μ_B and *ii*) we embed those newly derived dilepton rates in modern (3+1)-dimensional relativistic hydrodynamical simulations of heavy ion collisions. We focus our analysis on the invariant mass region $1 \text{ GeV} < M < 3 \text{ GeV}$ where QGP manifestations are expected to be prevalent [8, 31]. It will be seen that the presence of a nonzero μ_B modifies the quark and antiquark distributions in the QGP, and shifts the ther-

¹ See, however, the recent study of Ref. [9].

² Of course, the generation of electromagnetic probes from early

pre-equilibrium sources also deserves careful attention [12–18].

mal masses that control the associated screening effects. While the latter has been examined for real photons [32], in the first part of this paper we will present new results away from the light cone. This involves properly understanding how μ_B enters the strict NLO computation, how it affects the so-called Landau-Pomeranchuk-Migdal (LPM) effect, and how to smoothly interpolate between the two regimes as originally advocated in Ref. [33]. In addition, we also provide the dilepton yield's dependence on polarisation. The second part of our paper is devoted to integrating the new rates just discussed, using a realistic fluid dynamical simulation of the evolving medium.

Our work is organized as follows: the next section lays out general considerations pertaining to the evaluation of lepton pair production rates, and also sets up the general formalism needed for fluid dynamical simulations in environments with a net baryon number. Section III considers the different relativistic field theoretical aspects required to compute the photon self-energy at NLO in QCD in the presence of baryons, and we present the new dilepton rates. The following section, Section IV, discusses the phenomenology made possible by the measurement of lepton pairs at RHIC. We then summarize and conclude.

II. SETUP

A. Differential emission rate

To fix the notation, we denote the temperature by T , the quark chemical potential by μ and the energy and momentum of the lepton pair by ω and \mathbf{k} respectively.

$$E_+ E_- \frac{d\Gamma_{\ell\bar{\ell}}}{d^3\mathbf{p}_+ d^3\mathbf{p}_-} = \frac{f_B(\omega)}{2\pi^4 M^4} \left\{ \alpha_{\text{em}}^2 \sum_{i=1}^{n_f} Q_i^2 \right\} B\left(\frac{m_\ell^2}{M^2}\right) L^{\mu\nu} \rho_{\mu\nu}(\omega, k). \quad (2)$$

Here the Bose distribution function is $f_B(\omega)$, the quark charge-fractions are Q_i (in units of the electron charge), and the kinematic factor to produce the pair of leptons is $B(x) \equiv (1 + 2x)\Theta(1 - 4x)\sqrt{1 - 4x}$.

Equation (2) makes it clear that the photon spectral function is the central object of interest.³ Being the imaginary part of a retarded self energy, with averages taken in a thermal ensemble, $\rho_{\mu\nu}$ is intimately related to the Euclidean correlator—an object that can be estimated⁴ from continuum-extrapolated lattice data [37]. The resummed NLO spectral function holds

In chemical equilibrium, $\mu = \frac{1}{3}\mu_B$ where μ_B is the chemical potential associated with baryon number density n_B . For now, we consider ω and k to be defined by the local rest frame (LRF) of the plasma. We use a metric signature such that $K^2 \equiv K_\mu K^\mu = \omega^2 - \mathbf{k}^2$ is the invariant mass associated with the dilepton's four-momentum $K_\mu = (\omega, \mathbf{k})$.

The dilepton emission rate per unit volume, $\Gamma_{\ell\bar{\ell}}$, of an equilibrated QGP can be derived from the retarded photon self-energy, $\Pi_{\mu\nu}(\omega, \mathbf{k})$. It is the imaginary part of $\Pi_{\mu\nu}$ that defines a spectral function, which is thus *fully* characterised by two polarisations

$$\rho_{\mu\nu} \equiv \text{Im}[\Pi_{\mu\nu}] = \mathbb{P}_{\mu\nu}^L \rho_L + \mathbb{P}_{\mu\nu}^T \rho_T,$$

where we may take, e. g. , the following projectors in the fluid's LRF [34],

$$\mathbb{P}_{\mu\nu}^L = \frac{1}{K^2} \begin{pmatrix} \mathbf{k}^2 & \omega \mathbf{k} \\ \omega \mathbf{k} & \omega^2 \hat{k}_i \hat{k}_j \end{pmatrix}, \quad \mathbb{P}_{\mu\nu}^T = \begin{pmatrix} 0 & 0 \\ 0 & (\delta_{ij} - \hat{k}_i \hat{k}_j) \end{pmatrix}. \quad (1)$$

Of course, real photons satisfy $\omega = k \equiv |\mathbf{k}|$, whereas dileptons are issued forth by virtual photons with enough invariant mass $M \equiv \sqrt{\omega^2 - \mathbf{k}^2}$ to create two particles, each of mass m_ℓ , i. e. $M > 2m_\ell$. If the final state leptons carry four-momenta P_+ and P_- (so that $K = P_+ + P_-$), we define the associated leptonic tensor by $L^{\mu\nu} = P_+^\mu P_-^\nu + P_+^\nu P_-^\mu - g^{\mu\nu}(P_+ \cdot P_- + m_\ell^2)$. Then, to leading order in the electromagnetic fine-structure constant α_{em} and neglecting quark masses, the emission rate equals [35]

up to scrutiny when tested against lattice results for $n_f = \{0, 2\}$ [38, 39] and $n_f = 3$ [40] (all at zero μ_B), which motivates using the associated perturbative QCD rates to compute the actual yield from simulations.

The theoretical evaluation of the dilepton rate has a long history, with time and persistence having clarified most of the important physics issues. Initially, calculations assumed that the photon was at rest, i. e. $k = 0$, and $\omega \sim T$ which allowed the current-current correlator to be determined from the two-loop photon self energy [41–43]. It was soon recognised that such an approach breaks down for $\omega \lesssim \sqrt{\alpha_s} T$, where hard thermal loops (HTLs) [44] need to be resummed to account for screening and Landau damping [45, 46]. The same techniques were used to derive the photon rate ($\omega = k$), which is proportional to $2\rho_T$ and has the parametric behaviour $\omega d\Gamma_\gamma/d^3\mathbf{k} \sim \alpha_{\text{em}} \alpha_s \ln(1/\alpha_s) T^2$ [47, 48]. Spacelike vir-

³ Equation (2) is true to all orders in $\alpha_s = g^2/(4\pi)$ [36].

⁴ Information about $\rho_{\mu\nu}$ for *all* ω is needed to calculate the Euclidean correlator, while the dilepton rate only depends on the spectral function in the timelike region.

tualities ($\omega < k$) were only recently discussed in the literature, when first needed to connect with the Euclidean correlator—physically this concerns the somewhat academic case of deep inelastic scattering on a QGP target [49]. Whether the photon point is approached from above or below $K^2 \sim \alpha_s T^2$ (but keeping $\omega \sim T$) naively higher-order diagrams must be incorporated [50, 51]. In addition to HTL resummation, certain multiple scatterings are also mandated by collinear enhancement (the LPM effect) to rigorously give the leading⁵ QCD corrections [50, 54, 55]. The opposite limit, namely $M \gg T$, can be studied independently via the operator product expansion (OPE) [56].

A few extra considerations are needed to complete the calculation of $\rho_{\mu\nu}$ for $\mu_B \neq 0$, which we will describe in Sec. III, but no conceptual obstacles remain.

B. QGP spacetime evolution

Heavy-ion collisions are commonly described by multistage frameworks, which consist of a sequence of physical models to describe the evolution stages of the created systems [57, 58]. The hydrodynamic description of the deconfined QGP phase is the core of such frameworks. It describes the spacetime evolution of a system which is near local (chemical and thermal) equilibrium, with conservation of energy and momentum and that of baryon charge density [59, 60]:

$$\partial_\mu T^{\mu\nu} = 0, \quad \partial_\mu J_B^\mu = 0, \quad (3)$$

where $T^{\mu\nu}$ is the energy-momentum tensor and J_B^μ the net baryon charge current. In practice, the system of Eqs. (3) is solved numerically in coordinates where $\tau = \sqrt{t^2 - z^2}$ is the proper time and $\eta_s = \frac{1}{2} \ln \frac{t+z}{t-z}$ is the spacetime rapidity (with z being the Cartesian coordinate parallel to the beam direction).

We define the energy density e in the Landau frame, i.e. $u_\mu T^{\mu\nu} \equiv e u^\nu$, so that

$$T^{\mu\nu} = e u^\mu u^\nu - (p + \Pi) \Delta^{\mu\nu} + \pi^{\mu\nu}, \quad (4)$$

where $\Delta^{\mu\nu} \equiv g^{\mu\nu} - u^\mu u^\nu$, u^μ is the fluid four-velocity, $p + \Pi$ is the usual-plus-bulk viscous pressure, and $\pi^{\mu\nu}$ is the shear stress tensor. The baryon current reads

$$J_B^\mu = n_B u^\mu + q^\mu, \quad (5)$$

with n_B the local baryon number density and q^μ the associated diffusion current [59]. To close the system of

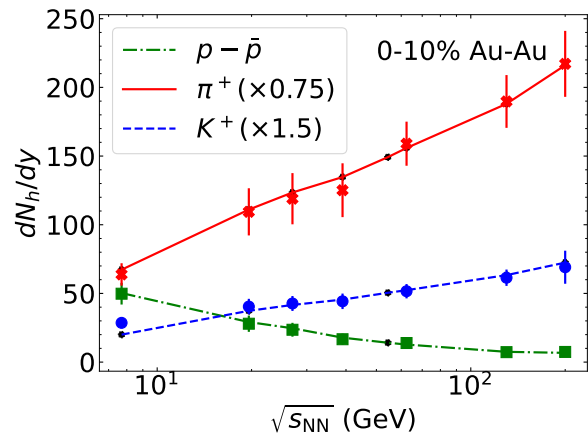


Figure 1. Identified hadron yields at midrapidity for 0-10% Au+Au collisions at eight beam energies from 7.7 to 200 GeV. The markers show the STAR measurements for net protons $p - \bar{p}$ (green square), pions π^+ (red cross), and kaons K^+ (blue circle) and the lines connect modeling results shown by black dots.

continuity equations for $T^{\mu\nu}$ and J_B^μ , one also requires the equation of state (EoS), i.e. $p = p(e, n_B)$, and a set of equations of motion for each of the dissipative currents Π , $\pi^{\mu\nu}$ and q^μ [61].

The pre-hydrodynamic stage becomes more complicated and important at lower collisional energies, where the Lorentz contraction of the nucleus is not sufficient to disregard the time it takes the two nuclei to entirely pass through one another. This is the case for the NA60+ experiments, which operate in the SPS energy range $5 \text{ GeV} < \sqrt{s_{NN}} < 17 \text{ GeV}$, and the Beam Energy Scan program at RHIC. We follow the initialisation procedure of Refs. [59, 62], which used an averaged Monte Carlo Glauber sampling for the initial conditions as input for hydrodynamic simulations starting at τ_0 . The hydrodynamical evolution, with dissipative corrections from $\pi^{\mu\nu}$ and q^μ [62], is simulated using the MUSIC fluid-dynamical approach [63, 64]. We use the equation of state NEOS-B [65] which neglects strangeness and electric charge chemical potentials.

The hydrodynamics evolves until $e_{f0} = 0.26 \text{ GeV}/\text{fm}^3$, to allow for a transient hot hadronic gas which is slightly cooler than the QGP. Once the hydrodynamic stage is complete, a freeze-out surface is generated and read into iS3D, a numerical simulation that uses the Cooper-Frye formalism to convert $T^{\mu\nu}$ into particles while conserving energy and momentum, and baryon charge. The subsequent hadronic re-scattering and resonance decays of the dilute phase are determined from UrQMD [67, 68]. The initial conditions are tuned so that the final hadron yields match the experimental measurements at midrapidity (see Fig. 1) and away from midrapidity if available (see Ref. [62]). Figure 2 depicts the hydrodynamic expansion trajectories (μ_B, T) in the phase diagram across three distinct spacetime rapidity windows for the two

⁵ In our convention, the LO spectral function refers to the QED result for $\rho_{\mu\nu}$ and the NLO spectral function includes the terms proportional to α_s . Papers that focus on the photon rate will refer to the latter as the ‘LO’ result because for $\omega \simeq k$ the process $q\bar{q} \rightarrow \gamma^*$ is kinematically suppressed and the spectral function starts with the QCD ‘corrections.’ Relative $\mathcal{O}(\sqrt{\alpha_s})$ terms in this limit have also been established [52, 53].

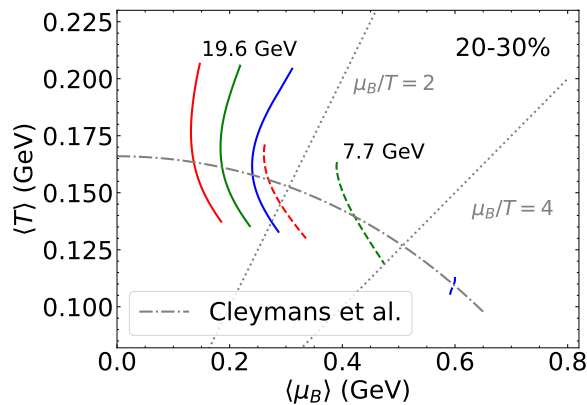


Figure 2. Hydrodynamic expansion trajectories in the phase diagram within three distinct spacetime rapidity windows $(-0.5, 0.5)$, $(0.5, 1.0)$, and $(1.0, 1.5)$ (from left to right curves) for 20-30% Au+Au collisions at 7.7 GeV (dashed lines) and 19.6 GeV (solid lines). The two dotted lines correspond to $\mu_B/T = 2$ and 4, respectively. The dot-dashed line represents the chemical freeze-out line from Ref. [66].

lowest beam energies. As shown in the figure, the created systems achieve higher chemical potentials and lower initial temperatures as the beam energy decreases, leading to shorter expansion trajectories, as observed at 7.7 GeV away from midrapidity. Notably, it reveals that, even at a beam energy of 7.7 GeV, a significant portion of fluid cells satisfies $\mu_B/T \lesssim 3$ within $|\eta_s| < 1$.

III. PERTURBATIVE RESULTS, $\mu \neq 0$

Before getting into the details, let us reiterate that our study is dedicated to the *equilibrium* thermal dilepton rate, i.e. we do not take into account any departure of the quark or gluon distribution functions from thermal and chemical equilibrium, as would occur in the presence of viscosity and/or diffusion.⁶ Although it has recently become clear how such corrections may be implemented, even when considering LPM-type diagrams [15, 27], we concentrate here on the changes brought about by including NLO and finite μ_B effects and leave off-equilibrium

considerations for future work.

According to the convention in Eq. (1), the longitudinal (L) and transverse (T) components can be expressed by

$$\rho_L = -\frac{K^2}{k^2}\rho_{00}, \quad \rho_T = \frac{1}{2}\left(\rho_\mu^\mu + \frac{K^2}{k^2}\rho_{00}\right). \quad (6)$$

We will denote the full trace by $\rho_V \equiv \rho_\mu^\mu = 2\rho_T + \rho_L$, which is needed for the dilepton rate. For the purpose of displaying formulas, it is simpler to focus on ρ_V and ρ_{00} .

For the spectral functions, the LO results are

$$\rho_V = \frac{N_c K^2}{4\pi k} \left\{ T \sum_{\nu=\pm\mu} \left[l_{1f}(k_+ - \nu) - l_{1f}(|k_-| - \nu) \right] + k\theta(k_-) \right\}, \quad (7)$$

$$\rho_{00} = \frac{-N_c}{12\pi k} \left\{ 12T^3 \sum_{\nu=\pm\mu} \left[l_{3f}(k_+ - \nu) - l_{3f}(|k_-| - \nu) \right] + 6kT^2 \sum_{\nu=\pm\mu} \left[l_{2f}(k_+ - \nu) + \text{sign}(k_-)l_{2f}(|k_-| - \nu) \right] + k^3\theta(k_-) \right\}, \quad (8)$$

where θ is the Heaviside step function and we have defined the polylogarithms

$$l_{1f}(x) \equiv \ln\left(1 + e^{-x/T}\right), \quad l_{2f}(x) \equiv \text{Li}_2\left(-e^{-x/T}\right), \\ l_{3f}(x) \equiv \text{Li}_3\left(-e^{-x/T}\right). \quad (9)$$

The function ρ_V (for $\mu \neq 0$) was previously determined in Ref. [69] for $\omega > k$. However, equation (7) and (8) are more general because they also hold for $\omega < k$. Setting $\mu = 0$ reproduces Eq. (2.4) from Ref. [38].

At NLO, the underlying spectral function can be reduced to a set of elementary ‘master integrals’ (many of which were studied for $\omega > k$ in [70]), providing a way to divide and conquer the otherwise very tedious calculation. The evaluation involves such integrals, whose imaginary parts are uniformly defined by

$$\rho_{abcde}^{(m,n)}(\omega, k) \equiv \text{Im} \left[\oint_{P,Q} \frac{p_0^m q_0^n}{[P^2]^a [Q^2]^b [(K-P-Q)^2]^c [(K-P)^2]^d [(K-Q)^2]^e} \right]_{k_0 \rightarrow \omega + i0^+}. \quad (10)$$

This spectral function corresponds to the generic two-loop topology for a self energy of external momentum K . In the sum-integrals,⁷ P and Q are fermionic momenta with $p_0 = i(2x+1)\pi T + \mu$ and $q_0 = i(2y+1)\pi T - \mu$ (where $x, y \in \mathbb{Z}$).

⁶ As mentioned in Sec. II B, corresponding effects are included in the hydrodynamic evolution.

⁷ To be crystal clear, with $d = D - 1$, the sum-integrals are:

$$\oint_P = \int_P T \sum_{p_0}; \quad \int_P = \left(\frac{e^\gamma \bar{\mu}^2}{4\pi}\right)^\epsilon \int \frac{d^d p}{(2\pi)^d}.$$

Turning now to the specific diagrams from Fig. 3, which we evaluate in $D = 4 - 2\epsilon$ spacetime dimensions, the result is a linear combination of the functions of the type (10). More specifically, the $\mathcal{O}(g^2)$ contributions read

$$\begin{aligned} \rho_{\text{V}}|_{\text{NLO}}^{(g^2)} &= 4(D-2)g^2 C_{\text{F}} N_{\text{c}} \left\{ (D-2) \frac{K^2}{2} \left(\rho_{11020}^{(0,0)} + \rho_{11002}^{(0,0)} - \rho_{10120}^{(0,0)} - \rho_{01102}^{(0,0)} \right) + \rho_{11010}^{(0,0)} \right. \\ &+ \rho_{11001}^{(0,0)} + (4-D) \rho_{11100}^{(0,0)} + 2 \frac{K^2}{k^2} \rho_{11011}^{(1,1)} - \frac{1}{2} K^2 \left(\frac{\omega^2}{k^2} + 7 - D \right) \rho_{11011}^{(0,0)} \\ &\left. - \frac{1}{2} (D-2) \left(\rho_{1111(-1)}^{(0,0)} + \rho_{111(-1)1}^{(0,0)} \right) + 2K^2 \left(\rho_{11110}^{(0,0)} + \rho_{11101}^{(0,0)} \right) - K^4 \rho_{11111}^{(0,0)} \right\}, \end{aligned} \quad (11)$$

$$\begin{aligned} \rho_{00}|_{\text{NLO}}^{(g^2)} &= 4g^2 C_{\text{F}} N_{\text{c}} \left\{ \frac{1}{2} (D-2) \left(\rho_{10110}^{(0,0)} + \rho_{01101}^{(0,0)} \right) + (4-D) \rho_{11100}^{(0,0)} + \left[\frac{1}{2} D K^2 - \omega^2 + 3k^2 \right] \rho_{11011}^{(0,0)} \right. \\ &- \frac{1}{2} (D-2) \left(4\rho_{11011}^{(1,1)} + \rho_{1111(-1)}^{(0,0)} + \rho_{111(-1)1}^{(0,0)} \right) + 2 \left[K^2 - (4-D)\omega^2 \right] \left(\rho_{11110}^{(0,0)} + \rho_{11101}^{(0,0)} \right) \\ &+ 2(4-D)\omega \left(\rho_{11110}^{(1,0)} + \rho_{11101}^{(1,0)} \right) - 2(D-2)\omega \left(\rho_{11110}^{(0,1)} + \rho_{11101}^{(0,1)} \right) \\ &\left. + \left[(D-3)\omega^2 + k^2 \right] K^2 \rho_{11111}^{(0,0)} + 2(4-D) K^2 \rho_{11111}^{(1,1)} - (D-2) K^2 \left(\rho_{11111}^{(2,0)} + \rho_{11111}^{(0,2)} \right) \right\}. \end{aligned} \quad (12)$$

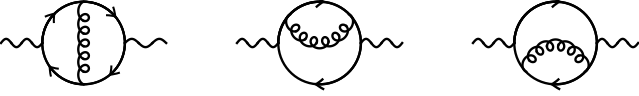


Figure 3. Strict two-loop contributions to the photon self-energy in QCD. (The 2nd and 3rd diagrams are distinct for $\mu \neq 0$.)

Above, the limit $D \rightarrow 4$ is implied because several of the master integrals have $1/\epsilon$ -divergences stemming from their vacuum parts. These all cancel when combined in the expressions above, but some care is required to verify that the result is finite [71]. In order to arrive at Eqs. (11) and (12), certain identities have been used to minimize the number of master integrals required. The same ‘minimal basis’ of functions was studied (for $\mu = 0$) in Refs. [70–72]. It is relatively straight forward to generalise those results to finite baryon densities; see Appendix A. Note that both Eq. (11) and Eq. (12) involve linear combinations which are symmetric in the simultaneous exchanges: $a \leftrightarrow b$, $d \leftrightarrow e$ and $m \leftrightarrow n$ for the master integrals. Consequently, the result will be unchanged by $\mu \rightarrow -\mu$. In the case where $\mu = 0$, using $\rho_{abcde}^{(m,n)} = \rho_{bacde}^{(n,m)}$ leads to the same decomposition as in Ref. [71], as expected.

A. Resummation in the LPM regime

The strict perturbative expansion is valid as long as $K^2 \gtrsim T^2$. In the opposite limit, i.e. $K^2 \rightarrow 0^\pm$, resummation is needed to obtain physically meaningful results. Thermal screening is the essential requirement, but the LPM effect also needs to be included for completeness. This has been well established at $\mu = 0$ [50, 54, 55]. At

non-zero baryochemical potential, results exist for the photon rate, $\omega = k$, which was considered in Ref. [73] and then the LPM effect was incorporated by Ref. [32]. Here we extend those results to $\omega \lesssim k$ (as well as studying ρ_{T} and ρ_{L} separately).

Two important scales in the problem are modified by the presence of a chemical potential: the Debye mass m_D and the ‘asymptotic’ quark mass m_∞ , *viz.*,

$$\begin{aligned} m_D^2 &\equiv g^2 \left[\left(\frac{1}{2} n_f + N_c \right) \frac{T^2}{3} + n_f \frac{\mu^2}{2\pi^2} \right], \\ m_\infty^2 &\equiv g^2 \frac{C_{\text{F}}}{4} \left(T^2 + \frac{\mu^2}{\pi^2} \right). \end{aligned} \quad (13)$$

For $K^2 \rightarrow 0^\pm$, the spectral function needs to be resummed in order to account for the LPM effect, with m_D and m_∞ being the key ingredients. In practice, kinematic approximations are invoked to perform the resummation to all orders for diagrams of the type shown in Fig. 4. Specifically, most formulations set up a two dimensional effective kinetic description in the transverse plane. Following the usual approach, we can express the spectral functions by

$$\begin{aligned} \rho_{00}|_{\text{LPM}}^{\text{full}} &\equiv -\frac{N_{\text{c}}}{\pi} \int_{-\infty}^{\infty} d\epsilon \left[1 - f_{\text{F}}(\epsilon - \mu) - f_{\text{F}}(\omega - \epsilon + \mu) \right] \\ &\times \int_{\mathbf{p}_\perp} \text{Im}[g(\mathbf{p}_\perp)], \end{aligned} \quad (14)$$

$$\begin{aligned} \rho_{\text{T}}|_{\text{LPM}}^{\text{full}} &\equiv -\frac{N_{\text{c}}}{\pi} \int_{-\infty}^{\infty} d\epsilon \frac{1 - f_{\text{F}}(\epsilon - \mu) - f_{\text{F}}(\omega - \epsilon + \mu)}{4\epsilon^2(\omega - \epsilon)^2} \\ &\times [\omega^2 - 2\epsilon(\omega - \epsilon)] \int_{\mathbf{p}_\perp} \text{Re}[\mathbf{p}_\perp \cdot \mathbf{f}(\mathbf{p}_\perp)], \end{aligned} \quad (15)$$

where the quantities g and \mathbf{f} are functions of the transverse momentum coordinate \mathbf{p}_\perp and satisfy the following

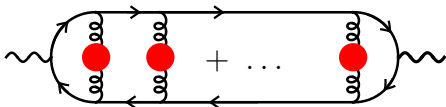


Figure 4. Class of diagrams that contribute in the LPM regime. Gluons have HTL resummed propagators and quarks are ‘hard,’ i.e. propagate with their asymptotic thermal mass.

integral equations⁸

$$2i = i\delta E g(\mathbf{p}_\perp) \quad (16)$$

$$+ g^2 C_F T \int_{\mathbf{q}_\perp} \mathcal{C}(\mathbf{q}_\perp) [g(\mathbf{p}_\perp) - g(\mathbf{p}_\perp - \mathbf{q}_\perp)],$$

$$2\mathbf{p}_\perp = i\delta E \mathbf{f}(\mathbf{p}_\perp) \quad (17)$$

$$+ g^2 C_F T \int_{\mathbf{q}_\perp} \mathcal{C}(\mathbf{q}_\perp) [\mathbf{f}(\mathbf{p}_\perp) - \mathbf{f}(\mathbf{p}_\perp - \mathbf{q}_\perp)].$$

The required collisional operator $\mathcal{C}(\mathbf{q}_\perp) = \frac{1}{q_\perp^2} - \frac{1}{q_\perp^2 + m_D^2}$ was found in Ref. [74]. On the right hand side of Eqs. (16) and (17), δE denotes an energy difference which accounts for the relative phase of the emitted radiation in the amplitude and conjugate amplitude. We shall explicitly define δE shortly.

It is convenient to solve the above integral equations in coordinate space, which leads to the two dimensional Schrödinger equations:

$$\begin{aligned} (\hat{H} + i0^+)g(\mathbf{y}) &= \delta^{(2)}(\mathbf{y}), \\ (\hat{H} + i0^+)\mathbf{f}(\mathbf{y}) &= -\nabla_\perp \delta^{(2)}(\mathbf{y}), \end{aligned} \quad (18)$$

where \mathbf{y} is a transverse coordinate. The boundary conditions are such that g and \mathbf{f} should be regular at the origin, where they are needed for Eqs. (14) and (15). In practice, we construct them from the S and P -wave solutions to the corresponding homogeneous differential equation as described in Ref. [33]. The operator $\hat{H} = \delta E + iV$ acts in the plane transverse to light-like propagation, with the potential

$$V = g^2 C_F T \int_{\mathbf{q}_\perp} (1 - e^{i\mathbf{y}\cdot\mathbf{q}_\perp}) \mathcal{C}(\mathbf{q}_\perp). \quad (19)$$

Before giving δE , let us recall that the LPM resummation assumes $\omega \gg gT$ and $K^2 = \omega^2 - k^2 \ll \omega^2$. Hence, certain terms may be exchanged, e.g. $k - \omega$ is equivalent to $-K^2/(2\omega)$ at this level of accuracy. The ambiguity starts to matter (numerically) when going beyond the presupposed strict kinematics. One can, however, mitigate this effect for practical purposes by maintaining a certain cancellation between the transverse and longitudinal polarisations that occurs at the Born level [33, 50].

⁸ A factor of $-i\sqrt{|\epsilon(\omega - \epsilon)|}$ is absorbed into the definition of g , compared with [51]. Our normalisation convention for g and \mathbf{f} matches Ref. [33].

We adopt this standard procedure, by multiplying ρ_{00} by K^2/ω^2 in (14) to obtain the longitudinal polarisation and to express the energy shift by

$$\delta E = -\frac{K^2}{2\omega} + \frac{1}{2} \left(\frac{1}{\epsilon} + \frac{1}{\omega - \epsilon} \right) (m_\infty^2 - \nabla_\perp^2). \quad (20)$$

The full spectral function can then be determined and the two projections ρ_i , with $i = T, L$, are given by

$$\begin{aligned} \rho_i|_{\text{LPM}}^{\text{full}} &\equiv -\frac{N_c}{\pi} \int_{-\infty}^{\infty} d\epsilon [1 - f_F(\epsilon - \mu) - f_F(\omega - \epsilon + \mu)] \\ &\times \lim_{\mathbf{y} \rightarrow \mathbf{0}} \left\{ \delta_{i,L} \frac{K^2}{\omega^2} \text{Im}[g(\mathbf{y})] \right. \\ &\quad \left. + \frac{\delta_{i,T}}{4} \left(\frac{1}{\epsilon^2} + \frac{1}{(\omega - \epsilon)^2} \right) \text{Im}[\nabla_\perp \cdot \mathbf{f}(\mathbf{y})] \right\}. \end{aligned} \quad (21)$$

B. How to combine NLO and LPM

As mentioned, the LPM regime relies on certain kinematic simplifications that only hold near the light cone. The strict NLO results involve general kinematics, but are plagued by an unphysical divergence as $K^2 \rightarrow 0^\pm$ which is precisely why resummation is needed there. We now discuss how these two formulations can be combined for ‘intermediate’ K^2 .

The resummed spectral functions ($i \in \{V, T, L, \dots\}$) are defined as [33]⁹

$$\begin{aligned} \rho_i|_{\text{NLO}}^{\text{resummed}} &\equiv \rho_i|_{1\text{-loop}}^{\text{strict}} + \rho_i|_{2\text{-loop}}^{\text{strict}} \\ &\quad + (\rho_i|_{\text{LPM}}^{\text{full}} - \rho_i|_{\text{LPM}}^{\text{expanded}}), \end{aligned} \quad (22)$$

where $\rho_i|_{1\text{-loop}}^{\text{strict}}$ is determined from Eqs. (7) and (8), $\rho_i|_{2\text{-loop}}^{\text{strict}}$ is determined from Eqs. (11) and (12), and $\rho_i|_{\text{LPM}}^{\text{full}}$ is given by Eq. (21). The quantity $\rho_i|_{\text{LPM}}^{\text{expanded}}$ is necessary for the ‘matching’ procedure and will be discussed in the next paragraph. Equation (22) is illustrated for $k = 2\pi T$ in Fig. 5, demonstrating that it is both finite and continuous across the light cone,

In order to combine the LPM and NLO results, we need to ‘re-expand’ the LPM results up to $\mathcal{O}(g^2)$ and remove double counting. This is because the full LPM spectral function contains one and two-loop diagrams under simplifying assumptions, which should rather be supplanted by the more correct LO and NLO results. At zeroth order in g , the expressions become

$$\begin{aligned} \rho_T|_{\text{LPM}}^{(g^0)} &= 2 \frac{N_c K^2}{\omega^2} \langle \epsilon^2 + (\omega - \epsilon)^2 \rangle, \\ \rho_L|_{\text{LPM}}^{(g^0)} &= 8 \frac{N_c K^2}{\omega^2} \langle \epsilon(\omega - \epsilon) \rangle, \end{aligned} \quad (23)$$

⁹ A more sophisticated way of interpolating was suggested in Ref. [75], and involves carefully modifying (20).

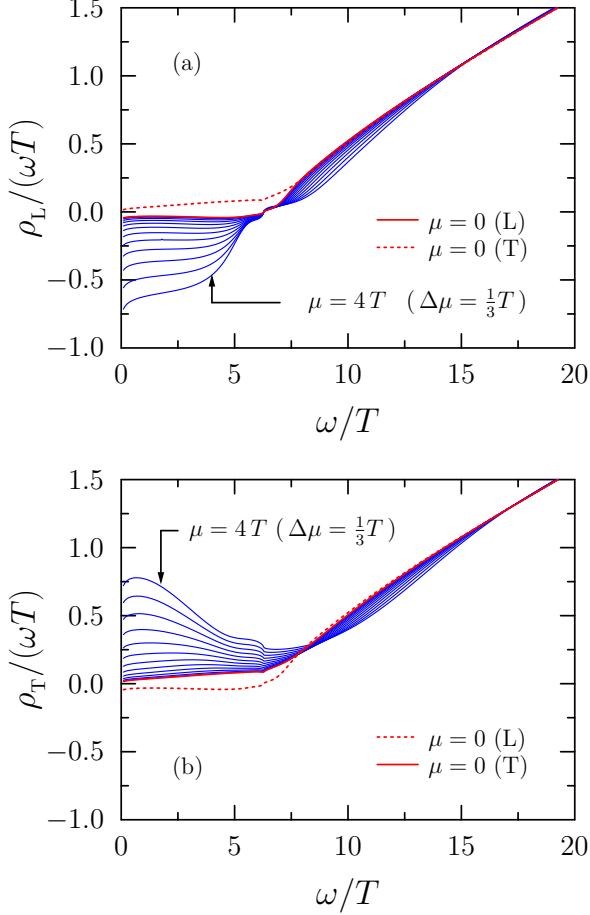


Figure 5. Transverse and longitudinal spectral functions, with $k = 2\pi T$ for a fixed value of the strong coupling $\alpha_s = 0.3$. The red curves in each figure depict $\rho_{T,L}$ for zero chemical potential. The solid lines depict ρ_L in panel (a) and ρ_T in panel (b). The family of blue curves indicates the effect of varying $\mu = 0, \dots, 4T$ in steps of $\Delta\mu = \frac{1}{3}T$.

where the angle brackets mean

$$\langle \dots \rangle \equiv \frac{1}{16\pi\omega} \left\{ \theta(K^2) \int_0^\omega d\epsilon - \theta(-K^2) \left[\int_{-\infty}^0 + \int_\omega^\infty \right] d\epsilon \right\} \times [f_F(\epsilon - \omega - \mu) - f_F(\epsilon - \mu)] (\dots). \quad (24)$$

These results should be compatible with Eqs. (7) and (8) in the small- K^2 limit, as confirmed by carrying out the explicit integration. The expressions can be represented in terms of

$$\langle \omega^2 \rangle = \frac{1}{16\pi} \left\{ \theta(K^2) \omega^2 + \omega T \sum_{\nu=\pm\mu} [l_{1f}(\omega - \nu) - l_{1f}(\nu)] \right\}, \quad (25)$$

$$\begin{aligned} \langle \epsilon(\omega - \epsilon) \rangle &= \frac{1}{32\pi} \left\{ \theta(K^2) \frac{\omega^2}{3} \right. \\ &+ 2T^2 \sum_{\nu=\pm\mu} [l_{2f}(\omega - \nu) + \text{sign}(K^2) l_{2f}(\nu)] \\ &\left. + 4 \frac{T^3}{\omega} \sum_{\nu=\pm\mu} [l_{3f}(\omega - \nu) - l_{3f}(\nu)] \right\}. \quad (26) \end{aligned}$$

The next corrections are of order g^2 , and are proportional to the asymptotic mass m_∞^2 . As in the $\mu = 0$ case [38], for ρ_L there is no such contribution for non-zero μ :

$$\rho_L|_{\text{LPM}}^{(g^2)} = 0. \quad (27)$$

However, the transverse spectral function ρ_T contains a logarithmic divergence, plus a finite part, namely

$$\begin{aligned} \rho_T|_{\text{LPM}}^{(g^2)} &= 2N_c m_\infty^2 \left\{ \left\langle 2 - \frac{\omega}{\epsilon_-} - \frac{\omega}{(\omega - \epsilon)_+} \right\rangle \right. \\ &+ \frac{1}{16\pi} \left[1 - f_F(\omega - \mu) - f_F(\omega + \mu) \right] \\ &\left. \times \left(\ln \left| \frac{m_\infty^2}{K^2} \right| - 1 \right) \right\}. \quad (28) \end{aligned}$$

We have introduced a convenient “ \pm notation” to regularize the two singularities appearing above,

$$\int d\epsilon \frac{f(\epsilon)}{\epsilon_-} \equiv \int d\epsilon \frac{f(\epsilon) - f(0)}{\epsilon}, \quad (29)$$

$$\int d\epsilon \frac{f(\epsilon)}{(\omega - \epsilon)_+} \equiv \int d\epsilon \frac{f(\epsilon) - f(\omega)}{\omega - \epsilon}. \quad (30)$$

For the resummation in Eq. (22) to be valid, it is crucial that the $\ln|K^2|$ term, evident in (28), is precisely cancelled by the NLO computation (11). This is shown analytically in Appendix B and is self-evident in the numerical results plotted in Fig. 5, which shows the longitudinal and transverse spectral functions as a function of the scaled energy, ω/T , for a fixed momentum $k/T = 2\pi$. This figure confirms the observation made in the case of real photons in Ref. [32], namely that the transverse spectral function at $\omega = k$ is enhanced by the presence of non-zero μ . For $\omega > k$, it appears that the chemical potential does not dramatically affect the spectral function compared to the $\mu = 0$ limit. Above the light cone point, there is a range of energies $k \lesssim \omega \lesssim 2k$ in which both ρ_T and ρ_L are slightly suppressed, although not as significantly as expected on the basis of the free result alone [69]. We note that for large- ω , the OPE predicts an overall enhancement of the rate due to

$$\rho_V \simeq \frac{N_c M^2}{4\pi} + 4g^2 C_F N_c \left\{ \frac{3M^2}{4(4\pi)^3} + \frac{\pi(\omega^2 + \frac{k^2}{3})}{36M^4} \left(T^4 + \frac{6}{\pi^2} T^2 \mu^2 + \frac{3}{\pi^4} \mu^4 \right) \right\}, \quad (31)$$

$$\rho_{00} \simeq -\frac{N_c k^2}{12\pi} - 4g^2 C_F N_c \left\{ \frac{k^2}{4(4\pi)^3} + \frac{\pi k^2}{108M^4} \left(T^4 + \frac{6}{\pi^2} T^2 \mu^2 + \frac{3}{\pi^4} \mu^4 \right) \right\}. \quad (32)$$

The neglected terms are of order $\mathcal{O}\left(\frac{T^6}{M^4}, \frac{T^4 \mu^2}{M^4}, \frac{T^2 \mu^4}{M^4}, \frac{\mu^6}{M^4}\right)$ and beyond. Therefore, in the large M^2 limit both the transverse and longitudinal rates will be *enhanced* by the presence of a chemical potential, which is just starting to be visible for $\omega \gtrsim 15T$ in Fig. 5 (although the effect is very small).

C. Setting physical units

From (2), we may calculate the fully differential production rate as a function of ω and \mathbf{k} by integrating over the direction of either \mathbf{p}_+ or \mathbf{p}_- . Assuming $n_f = 3$, with $Q_u = \frac{2}{3}$ and $Q_{d,s} = -\frac{1}{3}$, the rate becomes

$$\frac{d\Gamma_{\ell\bar{\ell}}}{d\omega d^3\mathbf{k}} = \frac{2\alpha_{\text{em}}^2 f_B(\omega)}{9\pi^3 M^2} B\left(\frac{m_\ell^2}{M^2}\right) \rho_V(\omega, \mathbf{k}), \quad (33)$$

where we used $K^\mu \rho_{\mu\nu} = 0$ to simplify the contraction with the leptonic tensor.¹⁰

Throughout this section (so far), we have made use of the scaling behaviour of the perturbative result:

$$\frac{\rho_i}{T^2} = \hat{\rho}_i\left(\frac{\omega}{T}, \frac{k}{T}, \frac{\mu_B}{T}; \alpha_s\right),$$

where $\hat{\rho}_i$ is a dimensionless function of dimensionless variables and we work with natural units ($\hbar = c = k_B \equiv 1$). Going over to physical units, we restore the factor $\text{GeV}^4 \text{fm}^4 \simeq 1/(0.197327)^4$ when displaying $d\Gamma_{\ell\bar{\ell}}/(d\omega d^3\mathbf{k})$ [72]. In addition, the perturbative parameter α_s is fixed in the rest of this work at $\alpha_s = 0.3$, a value consistent with that extracted from work devoted to RHIC phenomenology [77].

Let us start with the production rate in the local rest frame of a static thermal source before generalizing the discussion to an expanding inhomogeneous system. Presumably, the main features of the invariant mass spectrum

$$\frac{d\Gamma_{\ell\bar{\ell}}}{dM} = \int_{\mathbf{k}} \frac{M}{\sqrt{M^2 + k^2}} \frac{d\Gamma_{\ell\bar{\ell}}}{d\omega d^3\mathbf{k}}, \quad (34)$$

will carry over to more sophisticated circumstances.

The result of inserting (33) into (34) is shown in Fig. 6, which illustrates how the M -distribution is affected by T and μ_B . In this figure, the LO results from Eqs. (7) and

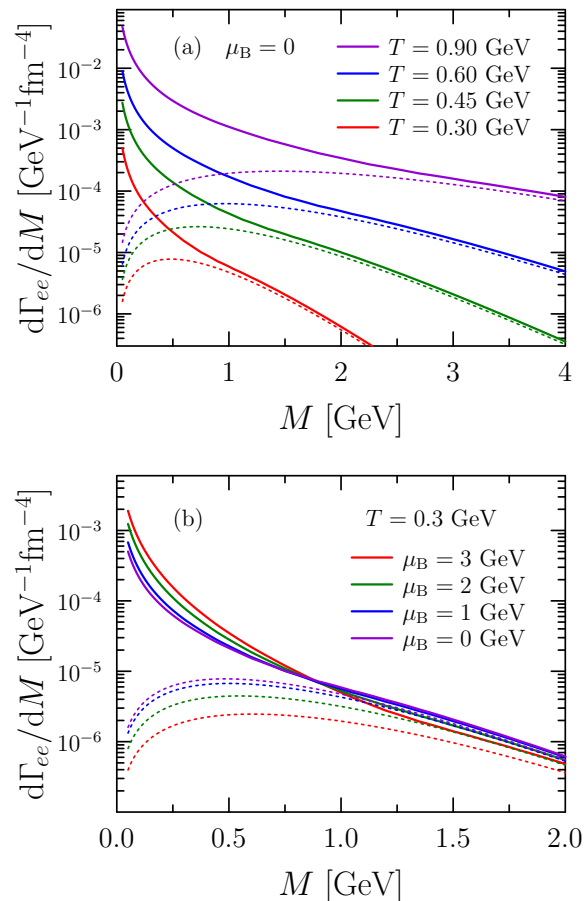


Figure 6. Thermal dilepton mass spectrum from a static source, for (a) $\mu_B = 0$ at several temperatures, and (b) for several values of μ_B at $T = 300$ MeV. The solid curves show the NLO rate with a fixed coupling $\alpha_s = 0.3$ and the dotted lines depict the rate due to the LO spectral function. In both plots, $n_f = 3$.

(8) are also shown to illustrate the relative importance of QCD corrections. We note the role T plays in the absolute magnitude of the rate, as expected for dimensional reasons. However, the impact of μ_B is more subtle: There is evidently some enhancement at low M when increasing μ_B , but this becomes a very mild *suppression* in the intermediate range. On the grounds of the LO result alone, one might conclude that adjusting μ_B to be different from zero leads to a depletion of quarks or antiquarks; thus fewer dileptons [69]. This effect is apparently partly mitigated at NLO by the effects of screening and the

¹⁰ The interpolation table of the emission rates is publicly accessible through the dilepton code used in this study [76].

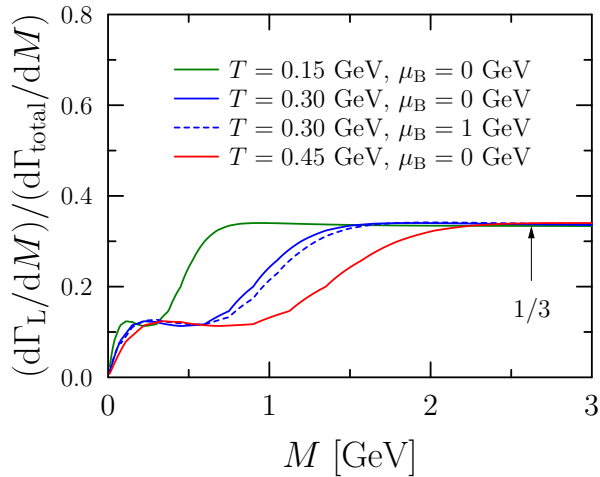


Figure 7. Fractional contribution of the longitudinal polarization to the total differential rate ($d\Gamma_{\text{total}} = 2d\Gamma_{\text{T}} + d\Gamma_{\text{L}}$) due to a point source Eq. (34). Note that for $M \rightarrow 0$ only the two transverse degrees of freedom contribute, whereas for large M the two spectral functions become equal: $\rho_{\text{T}} \approx \rho_{\text{L}}$.

LPM effect due to larger thermal masses (13).

Since both projections of the spectral function have been determined, we can decompose the (total) invariant mass distribution from (34) into its transverse and longitudinal components. This can be accomplished by simply replacing ρ_{V} with ρ_{T} or ρ_{L} in Eq. (33). The fraction contribution of the longitudinal polarization is shown in Fig. 7, for a thermal source at rest. Evidently, the two transverse components dominate the rate for low M but for highly virtual photons, $d\Gamma_{\text{L}} = d\Gamma_{\text{T}}$ and each contributes $\frac{1}{3}$ of the total rate. As Fig. 7 demonstrates, for temperatures and baryon densities of relevance, the latter situation is realized for $M \gtrsim 1$ GeV. Thus we shall not consider the polarizations separately in the rest of this paper, however it would be interesting to consider if the distinction could be made experimentally, perhaps from another observable derived from Eq. (2).

IV. DILEPTON PRODUCTION AT RHIC

A. Embedding rates in simulations

Observable spectra are determined by superimposing the differential rate in the LRF¹¹

$$\frac{dN_{\ell\bar{\ell}}}{dt d^3\mathbf{x} d\omega d^3\mathbf{k}} = \frac{d\Gamma_{\ell\bar{\ell}}}{d\omega d^3\mathbf{k}}, \quad (35)$$

¹¹ Here we assume the virtual photon's production takes place on time and distances smaller than those of the hydrodynamic evolution, and neglect finite-size effects on the scattering amplitudes.

on top of an expanding hydrodynamical background. The absolute yield is calculated from a spacetime integration over the QGP, which takes into account the local variation in its thermodynamic quantities $T \rightarrow T(t, \mathbf{x})$ and $\mu_{\text{B}} \rightarrow \mu_{\text{B}}(t, \mathbf{x})$ and the boost of $K_{\mu} = (\omega, \mathbf{k})$ to K'_{μ} by the fluid flow velocity $u^{\mu}(t, \mathbf{x})$; K'_{μ} is then the dilepton four-momentum in the lab frame. More explicitly, the emission rate in the lab frame is given by

$$\frac{dN_{\ell\bar{\ell}}}{d^4K'} = \int dt \int d^3\mathbf{x} \frac{d\Gamma_{\ell\bar{\ell}}}{d\omega d^3\mathbf{k}} \Big|_{K^{\mu} = \Lambda^{\mu\nu} K'_{\nu}}, \quad (36)$$

where $\Lambda^{\mu\nu}$ is the Lorentz transformation used to boost the lab frame four-momentum K'_{μ} to K_{μ} in the LRF of the fluid cell with four-velocity $u^{\mu}(t, \mathbf{x})$ ¹² [78, 79]. In practice, the spacetime integration is done by summing up contributions from discretized fluid cells. In this study, our primary focus is on thermal dileptons produced from the QGP. Therefore, we specifically consider the fluid cells with temperatures above the freeze-out line found in Ref. [66], as shown in Fig. 2. This line closely corresponds to the chemical freeze-out line as extracted by the STAR Collaboration [80]. Consequently, we attribute in this work the thermal dileptons emitted from the fluid cells below this line to contributions from hadronic matter.

Following the usual convention, we align the beam direction with the z -axis and introduce hyperbolic coordinates for the lab frame:

$$K'^{\mu} = (M_{\perp} \cosh y, \mathbf{k}_{\perp}, M_{\perp} \sinh y), \quad (37)$$

where $M_{\perp} \equiv \sqrt{M^2 + \mathbf{k}_{\perp}^2}$ is the transverse mass and y is the dilepton's rapidity (we omit the prime on \mathbf{k}_{\perp} , the transverse momentum, for brevity). Let ϕ be the azimuthal angle made by \mathbf{k}_{\perp} w.r.t. the z -axis. Using $d^4K' = M dM dy k_{\perp} dk_{\perp} d\phi$, the absolute dilepton yield is given by

$$\frac{dN_{\ell\bar{\ell}}}{dM dy} = M \int_{k_{\text{min}}}^{k_{\text{max}}} dk_{\perp} k_{\perp} \int_0^{2\pi} d\phi \frac{dN_{\ell\bar{\ell}}}{d^4K'}, \quad (38)$$

where k_{min} and k_{max} are set by detector acceptance. All the quantities involved in Eq. (38) are defined in the lab frame. The dilepton spectra within a rapidity window $y_{\text{min}} < y < y_{\text{max}}$ can be further obtained from

$$\frac{dN_{\ell\bar{\ell}}}{dM \Delta y} = \frac{1}{\Delta y} \int_{y_{\text{min}}}^{y_{\text{max}}} dy \frac{dN_{\ell\bar{\ell}}}{dM dy}, \quad (39)$$

where $\Delta y = y_{\text{max}} - y_{\text{min}}$ is the corresponding rapidity bin width¹³.

¹² In the simulation, the four-velocity vector $u^{\mu}(t, \mathbf{x})$ obtained from MUSIC is represented in Milne coordinates, while both K_{μ} and K'_{μ} are expressed in Cartesian coordinates. We perform a conversion of $u^{\mu}(t, \mathbf{x})$ from Milne coordinates to Cartesian coordinates to determine the boost transformation $\Lambda^{\mu\nu}$.

¹³ For the sake of brevity, we shall omit the $\ell\bar{\ell}$ subscript in $N_{\ell\bar{\ell}}$ from here on. The left-hand side of Eq. (39) is what is plotted as $dN/(dM dy)$ and $y_{\text{max/min}} = \pm 1$ unless noted otherwise.

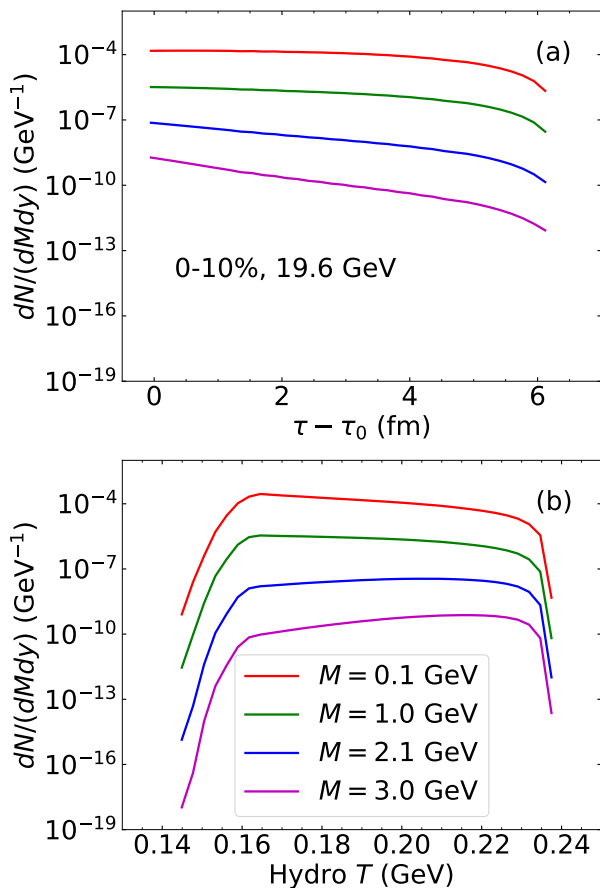


Figure 8. Evolution of dilepton yields with four different invariant masses as functions of (a) proper time (with τ_0 subtracted) and (b) simulation temperature for 0-10% Au+Au collisions at $\sqrt{s_{NN}} = 19.6$ GeV.

With the rapid hydrodynamic expansion, the QGP fireball undergoes a dramatic increase in volume and a substantial decrease in temperature. As illustrated in Fig. 6(a), the emission rate $d\Gamma_{\ell\bar{\ell}}/(d\omega d^3\mathbf{k})$ in Eq. (36) exhibits rapid decay as the temperature decreases, which stalls dilepton production as the system cools. However, simultaneously, the spacetime integration $\int d^4X$ increases with expanding volume, and thus bolsters the emission of dileptons. These two effects compete, resulting in distinct behaviors of the dilepton yields for various invariant masses emitted from the evolving QGP fireball, as illustrated in Fig. 8.

Figure 8(a) demonstrates that as time elapses, dilepton production is suppressed, primarily due to the decreasing emission rate resulting from the declining temperature, which prevails over the effect of the expanding volume. The suppression is also stronger for dileptons with larger invariant masses. However, when we organize the fluid cells based on their temperatures, calculate the dilepton yields contributed by cells at these temperatures, and then plot the dilepton yields as a function of temperature in Fig. 8(b), we observe distinct behav-

iors for different invariant masses in three temperature ranges. Dileptons originating from the high-temperature region ($T \gtrsim 0.23$ GeV) are primarily emitted by fluid cells at the earliest stage of the evolution with the highest energy density. Conversely, those from the low-temperature region ($T \lesssim 0.16$ GeV) are radiated from cells near the chemical freeze-out temperature, mostly from the latest stage of the evolution. The yields exhibit a significant suppression when the temperature decreases to approximately $T \approx 0.16$ GeV. This occurs because the fluid cells near midrapidity ($\eta_s \approx 0$), which are the primary contributors to dileptons within $|y| < 1$, cross the freeze-out line (see Fig. 2). Below $T \lesssim 0.16$ GeV, most dileptons originate from fluid cells located away from midrapidity, characterized by higher chemical potentials and consequently lower freeze-out temperatures. Dileptons from these cells with larger spacetime rapidities can still be observed within $|y| < 1$, because of ‘thermal smearing,’ as discussed in the next section (and in Appendix C). As shown in Fig. 8(b), dileptons produced in these two regions contribute sub-dominantly compared to those from the intermediate temperature range ($0.16 \text{ GeV} \lesssim T \lesssim 0.23 \text{ GeV}$). In this range, we observe an enhancement in dileptons with small masses and a suppression in those with large masses as the temperature *decreases*. This suggests that, in certain temperature ranges, the expanding volume may dominate over the decreasing emission rate for small masses. To appreciate Fig. 8(b), it’s important to note that fluid cells with lower temperatures predominantly correspond to later stages of the evolution, which generally have larger volumes.

B. Dependence on chemical potential and rapidity

Figure 6(b) illustrates the weak μ_B -dependence of the emission rate. It is valuable to investigate the corresponding μ_B -dependence of the dilepton spectra for the baryon-charged QGP, as brought up in Sec. II B. This analysis can help to answer whether experimentally measured dileptons can effectively serve as a baryometer. For this purpose, we compute the dilepton invariant mass spectra at the two lowest beam energies (with the highest μ_B) under two distinct scenarios: *i*) a μ_B -dependent emission rate and *ii*) with μ_B manually set to zero in the rate. Figure 9 presents a comparison between these two scenarios for 40-50% Au+Au collisions at 7.7 and 19.6 GeV. The analysis demonstrates that the μ_B -dependence is relatively minimal and not resolvable with the current measurement precision. This is because even μ_B/T achieved at 7.7 GeV is relatively small compared to the cases in Fig. 6(b), as shown in Fig. 2. The results illustrate that the total dilepton yields within rapidity window $|y| < 1$ are not a good baryometer for the systems produced in collisions at $\sqrt{s_{NN}} \gtrsim 7.7$ GeV.

Another significant feature of low collision energies, in addition to the nonzero baryon chemical potential, is the strong violation of Bjorken boost invariance. This viola-

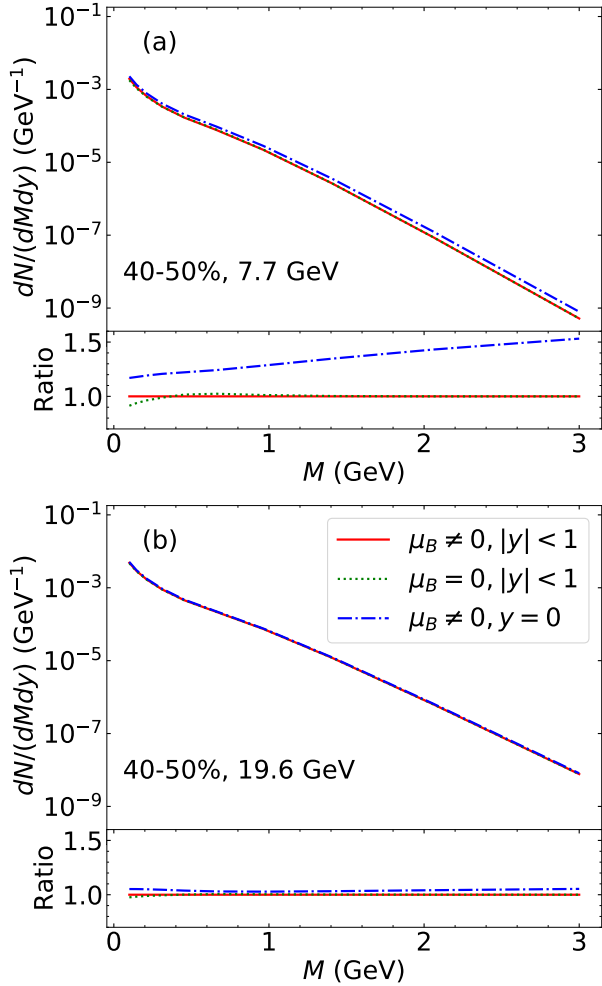


Figure 9. Dilepton invariant mass spectra for 40-50% Au+Au collisions at (a) $\sqrt{s_{\text{NN}}} = 7.7$ GeV and (b) $\sqrt{s_{\text{NN}}} = 19.6$ GeV presented in three scenarios: *i*) Spectra within a rapidity window $|y| < 1$ with μ_B -dependent emission rates (red solid line). *ii*) Spectra within a rapidity window $|y| < 1$ with μ_B manually set to zero in the rate (green dotted line). *iii*) Spectra at midrapidity $y = 0$ with μ_B -dependent emission rates (blue dot-dashed line). The bottom panels display the ratios of the spectra with the first scenario as the denominator.

tion is anticipated to be most pronounced at the lowest beam energies, manifesting as stronger flow and more significant variations in thermodynamic properties along the beam direction [62, 81]. To investigate the impact of boost-non-invariant effects on dilepton production and assess the validity of the midrapidity spectra as an approximation for a rapidity window $|y| < 1$, we have additionally computed the spectra at midrapidity $y = 0$ while considering μ_B -dependent emission rates. The ratio of the spectrum in this case to the one within $|y| < 1$ exhibits a significant enhancement at 7.7 GeV, reaching an excess as high as 50%, and a more modest enhancement at 19.6 GeV, for which the relative excess is $\lesssim 10\%$. We have checked that this enhancement gradually diminishes

at higher beam energies. This indicates the significance of boost-non-invariant effects on dilepton production at beam energies $\sqrt{s_{\text{NN}}} \lesssim 10$ GeV. Furthermore, it suggests that at beam energies above tens of GeV, the spectra at midrapidity $y = 0$ serve as a suitable approximation for a rapidity window $|y| < 1$. It's also intriguing to observe that the enhancement exhibits a dependence on the invariant mass, with a smaller effect for smaller masses. This behavior is attributable to the fact that the dilepton yield experiences more significant thermal smearing in rapidity for smaller masses (see Appendix C). Consequently, the yields at midrapidity $y = 0$ and within a rapidity window $|y| < 1$ begin to coincide for smaller masses.

C. Temperature extraction from dilepton spectra

The dilepton invariant mass spectrum remains the same under change of reference frame, which means it remains unaltered by the collective expansion of the medium¹⁴. Consequently, unlike the transverse momentum spectra of photons, the dilepton mass spectrum does not experience a blue shift and thus is often considered a reliable thermometer of the QCD fireball [8, 82]. Therefore, measurements of real and virtual photons can be combined to constrain both the local and global behaviour of the strongly interacting medium.

In the limit $M \gg T$ and μ_B , the LRF emission rate can be approximated by

$$\frac{d\Gamma_{\ell\bar{\ell}}}{dM} \propto (MT)^{3/2} \exp(-M/T). \quad (40)$$

Assuming the spacetime-integrated spectrum (see Fig. 9) exhibits a similar form, an effective temperature T_{eff} can be extracted from it. Importantly, this temperature is termed “effective” because the evolving fireball is highly dynamic and inhomogeneous and the final spectrum contains dileptons that are produced at different times and temperatures, as illustrated in Fig. 8. With access to the true temperature through hydrodynamic evolution, we can test this extraction method and gain insights on the effective temperature by contrasting its values obtained from the spectra with the temperatures of the fluid cells responsible for these spectra.

In practice, we determine T_{eff} from the inverse slope of $\ln[(dN/dM)M^{-3/2}]$. (The factor $M^{-3/2}$ is included to enhance the linearity with respect to M in a log-linear plot.) We will make use of dileptons with a mass range of $1 \text{ GeV} < M < 3 \text{ GeV}$, which are predominantly generated by the QGP; lower invariant masses will get important contributions from reactions involving composite hadrons [83] which are not included in this study. In this mass

¹⁴ Strictly speaking, y can still cause $dN/(dMdy)$ to become modified under a change of reference frame.

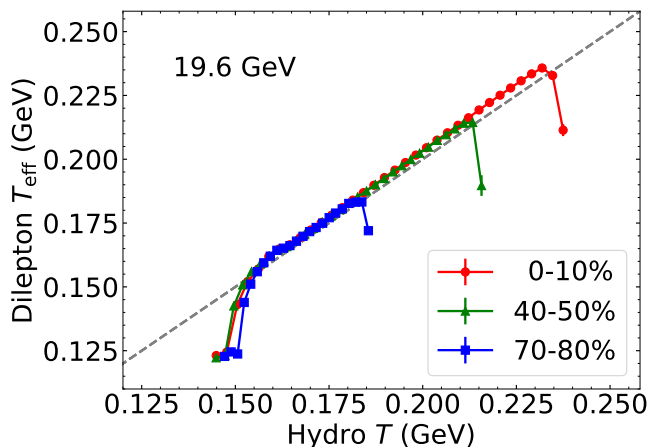


Figure 10. Effective temperature T_{eff} read off dilepton spectrum (“dilepton T_{eff} ”) emitted from fluid cells at different temperatures (“hydro T ”) for Au+Au collisions at $\sqrt{s_{\text{NN}}} = 19.6$ GeV within three centrality classes. The two temperatures are exactly equal on the grey dashed line.

range, Eq. (40) can be used as an ansatz (the suitability of which can be tested by comparing the “average” simulation T with T_{eff}).

In Fig. 8(b), we have computed dilepton spectra produced from fluid cells categorized by their respective temperatures. Using the temperature extraction method described above, we can obtain an effective temperature from the dilepton spectrum (“dilepton T_{eff} ”) corresponding to each fluid temperature (“hydro T ”), and their comparison is shown in Fig. 10. In the temperature range $0.16 \text{ GeV} \lesssim T \lesssim 0.23 \text{ GeV}$, we note that the two temperatures are remarkably similar, suggesting that the temperature extraction method performs well.¹⁵ However, small deviations can be observed which may arise due to several factors. First, Eq. (40) used for temperature extraction only represents an approximation. Second, each “hydro T ” corresponds to a finite temperature range (of bin width $\Delta T \simeq 0.002 \text{ GeV}$) rather than a precise value. Thirdly, even when the fluid cells share the same temperature, they have different proper times in the evolution and thus possess different volumes. These factors spoil the idealization above and introduce further complexities into the invariant mass spectra. As previously discussed in Sec. IV A, dileptons emitted from the high-temperature region ($T \gtrsim 0.23 \text{ GeV}$) and the low-temperature region ($T \lesssim 0.16 \text{ GeV}$) originate from fluid cells with the highest energy densities or those near the chemical freeze-out temperature, respectively. Although the deviations in these regions are slightly more pronounced, the contributions from fluid cells within the

¹⁵ In terms of the physics involved, this may seem somewhat straightforward; however, from a computational perspective, it represents a highly intricate validation of the numerical implementation of our entire framework.

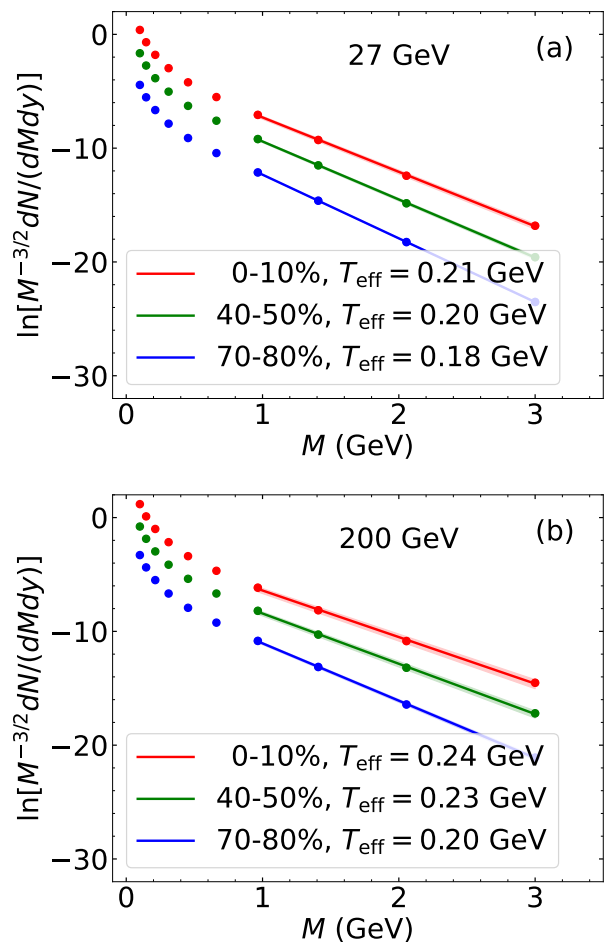


Figure 11. Effective temperature extraction from dilepton spectrum for Au+Au collisions at (a) $\sqrt{s_{\text{NN}}} = 27$ GeV and (b) $\sqrt{s_{\text{NN}}} = 200$ GeV within three centrality classes. The straight lines represent the linear fit function in the mass window $1 \text{ GeV} \leq M \leq 3 \text{ GeV}$, with their inverse slope providing the effective temperature T_{eff} . The shaded band indicates the uncertainties associated with the fitting procedure.

range $0.16 \text{ GeV} \lesssim T \lesssim 0.23 \text{ GeV}$ dominate the dilepton production.

With the temperature extraction method validated across various fluid cell temperatures, we proceed to apply the method to the spacetime-integrated dilepton spectra produced throughout the entire evolution and determine an effective temperature for the expanding fireball. Evidently, the resulting T_{eff} would represent an average over the temperatures of fluid cells above the freeze-out line. Figure 11 illustrates this implementation, using dileptons with $1 \text{ GeV} \leq M \leq 3 \text{ GeV}$ for temperature extraction. In the plot, the dots correspond to the model calculations, and the lines represent the linear fit functions. The inverse slope of the fit function provides the value of T_{eff} . The shaded band in the figure represents the uncertainties resulting from the fitting procedure, consequently leading to uncertainties in T_{eff} . It’s noteworthy that the linear fit performs exceptionally well within the

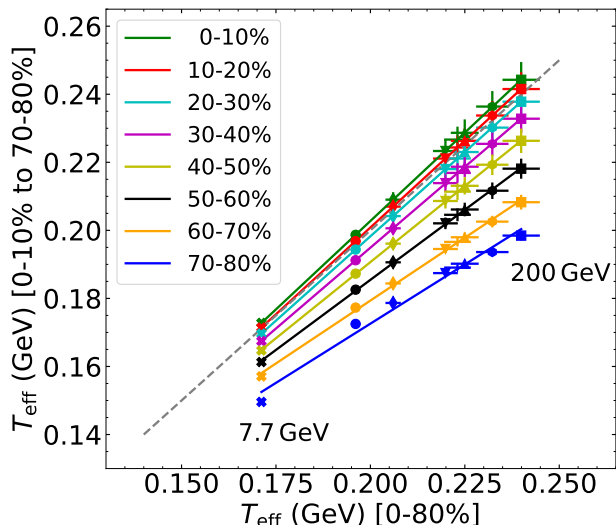


Figure 12. Effective temperature T_{eff} derived from dilepton spectra for Au+Au collisions at eight beam energies from $\sqrt{s_{\text{NN}}} = 7.7$ GeV (leftmost markers) to 200 GeV (rightmost markers). Horizontal coordinates of the markers represent T_{eff} from the minimum-bias collisions (0-80%), while vertical coordinates show T_{eff} within smaller centrality bins (0-10%, 10-20%, ..., 70-80%). Error bars denote associated uncertainties, and straight lines represent linear fits applied to the markers.

log-linear plot, strongly indicating that the approximate expression in Eq. (40) is indeed a reasonable approximation, with the exponential term $\exp(-M/T)$ playing a dominant role in the mass window $1 \text{ GeV} \leq M \leq 3 \text{ GeV}$.

Using the extraction method, an effective temperature can be derived from a dilepton spectrum of a system at any beam energy within a given centrality class. We calculate the dilepton spectra for Au+Au collisions at the eight beam energies studied in this work, considering centrality bins ranging from 0-10% to 70-80%, as well as the minimum-bias 0-80% centrality class which aligns with the experimentally measured centrality by STAR [84–87]. The agreement between our calculated spectra and experimental data in the minimum-bias events is discussed in the companion Letter [88]. Effective temperatures derived from these spectra are shown in Fig. 12. In the plot, the horizontal coordinates of the markers illustrate T_{eff} values obtained from the minimum-bias collisions, while the vertical coordinates display T_{eff} values within narrower centrality bins.

The figure shows that, within a specific centrality bin, T_{eff} decreases at lower beam energies, while at a given beam energy, T_{eff} decreases as one moves from central to peripheral collisions. Naturally, these observations are in line with the expectation, as they simply reflect the characteristics of the hydrodynamic evolution constrained by the hadron yields, which was previously discussed in Sec. II B. It's worth highlighting the intriguing observation that the T_{eff} values obtained from minimum-

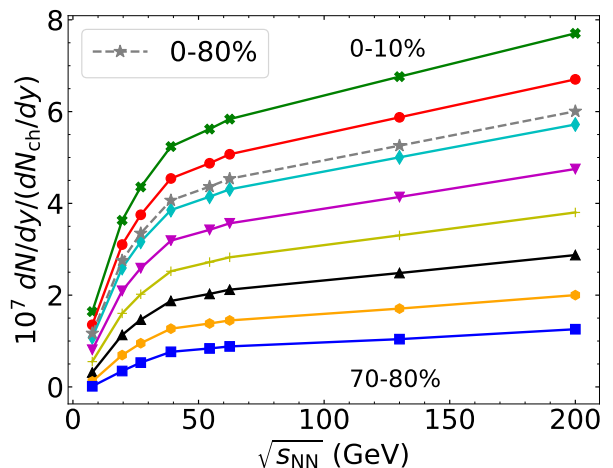


Figure 13. Integrated dilepton yields in the mass range $1 \text{ GeV} \leq M \leq 3 \text{ GeV}$, normalized by midrapidity charged hadron multiplicity (dN_{ch}/dy), for Au+Au collisions at eight beam energies spanning from $\sqrt{s_{\text{NN}}} = 7.7$ GeV (leftmost markers) to 200 GeV (rightmost markers). Results are presented within centrality classes ranging from 0-10% (uppermost curve) to 70-80% (lowermost curve), in 10% increments. The dashed line represents results within centrality class 0-80%.

bias collisions at varying beam energies fall between the 10-20% and 20-30% centrality collisions, with a closer alignment to the 10-20% values. This is indeed expected, as the dilepton production in minimum-bias collisions is dominated by central collisions. Verifying this observation in future experimental measurements, especially when statistical precision is sufficient, could serve as a critical test of the physics incorporated in this study.

Figure 12 illustrates a consistent trend: uncertainties in T_{eff} rise with increasing beam energy within a specific centrality class, or from peripheral to central collisions at a given beam energy. This trend can also be seen in the results presented for the two specific beam energies shown in Fig. 11. One contributing factor to this trend is the prolonged lifetime of the fireball at higher beam energies or central collisions, coupled with more significant temperature variations during its evolution. Consequently, the dilepton spectra exhibit more pronounced deviations from those associated with a particular effective temperature. This phenomenon is likely the main source of the increased uncertainties in T_{eff} extraction.

D. Integrated yields and fireball lifetime

The dilepton yields in the low-mass region ($M \lesssim 1 \text{ GeV}$) are thought to correlate with the total lifetime of the nuclear fireball [8, 86]. In that region, dilepton production is dominated by hadronic sources which are not within the scope of this study. Therefore, we investigate the relationship between thermal yields in the intermediate mass region, dominated by QGP thermal radiation,

and the duration of the QGP stage as determined by our realistic hydrodynamic modeling.

In Fig. 13, we present integrated dilepton yields within the mass range of $1 \text{ GeV} \leq M \leq 3 \text{ GeV}$, normalized by midrapidity charged hadron multiplicity (dN_{ch}/dy). We estimate dN_{ch}/dy by the dN/dy sum of π^\pm , K^\pm , p and \bar{p} obtained from the model calculation, following the STAR measurements. The figure illustrates a clear trend: within a specific centrality class, the yield decreases at lower beam energies, and does so more rapidly in central than in peripheral collisions. Similarly, at a given beam energy, the yield decreases from central to peripheral collisions. These trends are consistent with our expectations regarding the QGP stage's lifetime. The results for the 0-80% centrality class are also displayed, and they fall between the results for the 10-20% and 20-30% centrality classes, with a closer alignment to the latter. This observation is similar to what we've noticed regarding the effective temperatures shown in Fig. 12, with the exception that the effective temperatures of the 0-80% centrality appear closer to those of the 10-20% centrality.

The QGP stage's lifetime, denoted as τ_{QGP} , is calculated as the difference between τ_{fo} (the time when the temperatures of all fluid cells within $|\eta_s| < 1$ reach the chemical freeze-out line) and τ_0 (the starting time of the hydrodynamic description). This corresponds to the time range covered by the fluid cells contributing to the thermal dilepton yields, defined as the difference between the maximum and minimum times associated with all fluid cells. The correlation between normalized integrated dilepton yields and QGP lifetimes is depicted in Fig. 14. In this plot, results within distinct centrality classes at a given beam energy are connected by lines for clarity. The figure illustrates a roughly linear relationship between normalized integrated dilepton yields and QGP lifetimes at specific beam energies $\sqrt{s_{\text{NN}}} \geq 19.6 \text{ GeV}$; however, it's important to note that this proportionality is not consistent across all beam energies.

At $\sqrt{s_{\text{NN}}} = 7.7 \text{ GeV}$, a notably different trend is manifest in Fig. 14. Firstly, unlike the rough linearity observed at higher energies, the correlation at 7.7 GeV is more complicated. Secondly, within specific centrality classes, we notice a systematic decrease in the QGP stage's lifetime with decreasing beam energy, which remains consistent until 19.6 GeV. At 7.7 GeV, the system features a high chemical potential corresponding to a low chemical freeze-out temperature (see Fig. 2). This, combined with the notably slower expansion at lower beam energies, leads to a prolonged duration required to reach the freeze-out line and thus a longer QGP lifetime. However, it is important to emphasize that defining the QGP lifetime becomes challenging at such low beam energies because of the long time needed for the two colliding nuclei to interpenetrate each other. In principle, at these low energies a dynamical initialization process would be necessary, which goes beyond the scope of the present study.

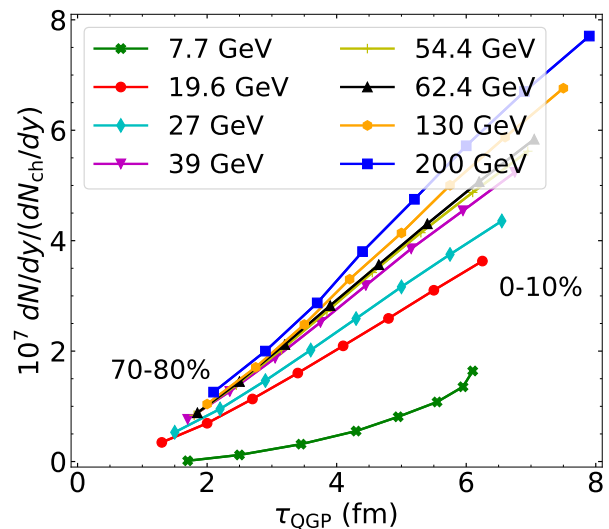


Figure 14. Correlation between normalized integrated dilepton yields and QGP lifetimes in Au+Au collisions at eight beam energies, ranging from $\sqrt{s_{\text{NN}}} = 7.7 \text{ GeV}$ (lowest curve) to 200 GeV (highest curve), across centrality classes from 0-10% (rightmost markers) to 70-80% (leftmost markers).

V. SUMMARY AND CONCLUSION

We have derived rates for thermal dilepton production at NLO in the QCD coupling constant, for partonic matter at finite temperature and finite baryon density. The establishment of those rates necessitated considering the contribution of the two-loop photon self-energy diagrams, combined with the re-summed class of diagrams that represent the LPM effect. The new spectral functions obtained from the two-loop topologies are Eqs. (11) and (12). When combining strict one and two-loop results with the LPM effect, first advocated by Ref. [33], close attention was paid to double-counting issues, and a spectral function which is finite and continuous across the light cone was obtained. The thermal rates for lepton pair production exhibit a large sensitivity to NLO corrections which translates into a large enhancement over the LO result at low invariant masses. These effects still persist in the intermediate mass domain, depending on the probed temperature. The inclusion of a baryon chemical potential boosts the dilepton rates at low masses. For intermediate masses, the rates with larger μ_B are suppressed with respect to those with smaller values, but to a lesser extent than what is found at LO.¹⁶ We have also highlighted the marked difference between the transverse and longitudinal components of the dilepton emission rates, in Fig. 7. The phenomenology resulting from

¹⁶ In the large M limit, the OPE results, Eqs. (31) and (32), predict an enhancement of the dilepton thermal rates, which however remains modest for the invariant masses and temperatures considered in this work.

this will be explored in detail in future work, as will be the effects on the rates of viscosity corrections.

The second part of our paper is devoted to going from rates to yields, using a modern fluid-dynamical approach which has been calibrated to reproduce hadronic observables. The temperatures extracted from the slope of the dilepton spectrum for invariant masses M such that $1 \text{ GeV} < M < 3 \text{ GeV}$, have been compared with those in the hydrodynamic simulation for Au+Au collisions at different energies and centralities (Fig. 10). This investigation with (3+1)-dimensional viscous fluid dynamics finds that measurements of thermal lepton pairs offer a quantitative assessment of the temperature (Figs. 11 and 12) of the QCD medium [88] as well as its lifetime (Figs. 13 and 14). Its baryonic content is more difficult to extract from dileptons, but future measurements with the capacity to extract polarization signature could provide further information.

In addition to its ability to provide temperature information, the intermediate invariant mass domain has been identified as a promising region in which to look for signals of chiral symmetry restoration¹⁷ [90]. These studies make it clear that a precise characterization of the strongly interacting medium via electromagnetic radiation requires state-of-the-art emissivities, integrated with sophisticated modeling.

ACKNOWLEDGMENTS

We are happy to acknowledge very useful discussions with Bailey Forster, Han Gao, and Jean-François Paquet. This work was funded in part by the U. S. Department of Energy (DOE), under Grant No. DE-FG02-00ER41132 (G. J.), in part by the Agence Nationale de la Recherche, under Grant No. ANR-22-CE31-0018 (AUTOTHERM) (G. J.), and in part by the Natural Sciences and Engineering Research Council of Canada (J. C., L. D., C. G., S. J.). Computations were made on the Béluga super-computer system from McGill University, managed by Calcul Québec and Digital Research Alliance of Canada.

Appendix A: Master integrals

In Ref. [91], the types of interactions that would contribute to NLO rates were studied (with full generality) and a numerical routine for *any* combination of particles, masses, chemical potentials and a wide class of matrix elements was developed. For the dilepton rate, it is preferable to use a more tailored approach which requires a

two-dimensional phase space integration [71]. This applies, specifically, to the master integrals introduced in Eq. (10) for which the code can be found at Ref. [92].

To account for non-zero μ , the abbreviations defined in Eq. (6.3) of Ref. [71] (where $n_s(\omega) \equiv [\exp(\omega/T) - s]^{-1}$) should be generalised to the following:

$$\begin{aligned} n_0 &= s_0 n_{s_0}(\omega) & , & \\ n_1 &= s_1 n_{s_1}(p - \mu_1) & , & \\ n_2 &= s_2 n_{s_2}(q - \mu_2) & , & \\ n_3 &= s_3 n_{s_3}(r - \mu_3) & ; & \quad r = \omega - p - q, \\ n_4 &= s_4 n_{s_4}(\ell - \mu_4) & ; & \quad \ell = \omega - p, \\ n_5 &= s_5 n_{s_5}(v - \mu_5) & ; & \quad v = \omega - q. \end{aligned} \quad (\text{A1})$$

If the particles are in chemical equilibrium, the potentials are constrained by linear relations: $\mu_3 = -\mu_1 - \mu_2$, $\mu_4 = -\mu_1$ and $\mu_5 = -\mu_2$.

Of relevance to dilepton production, particles ‘1’ and ‘4’ are quarks with $\mu_1 = \mu_4 = \mu$, particles ‘2’ and ‘5’ are anti-quarks with $\mu_2 = \mu_5 = -\mu$ and particle ‘3’ is a gluon ($\mu_3 = 0$). The statistical factors are thus $s_0 = s_3 = +1$ and $s_1 = s_2 = s_4 = s_5 = -1$. For our purpose, we specify (A1) with the replacements,

$$\begin{aligned} n_0 &\rightarrow +f_{\text{B}}(\omega), & n_1 &\rightarrow -f_{\text{F}}(p - \mu), \\ n_2 &\rightarrow -f_{\text{F}}(q + \mu), & n_3 &\rightarrow +f_{\text{B}}(r), \\ n_4 &\rightarrow -f_{\text{F}}(\ell + \mu), & n_5 &\rightarrow -f_{\text{F}}(v - \mu). \end{aligned} \quad (\text{A2})$$

The master integrals defined in (10) can be studied independently within the HTL approximation, and we have checked our result in this limit [39].

Appendix B: Matching of IR-singularities near the light cone

For (22) to make sense, we expect that the (subtracted) singularity in (28) is compensated by the strict two-loop result in (11) and (12) to render the functions non-singular.

We focus on ρ_{V} , but the same can be done for ρ_{00} . In (11), the discontinuous terms are $\rho_{11010}^{(0,0)}$ and $\rho_{1111(-1)}^{(0,0)}$ (the latter also being responsible for the log divergence). Following Ref. [71], we express $\rho_{1111(-1)}^{(0,0)} = \rho_{10110}^{(0,0)} + K^2 \rho_{11110}^{(0,0)} - \rho_{11110}^*$. Therefore, since $\rho_{11110}^{(0,0)}$ is continuous at $\omega = k$,

$$\begin{aligned} \rho_{\text{V}}|_{\text{disc}} &= 8g^2 C_{\text{F}} N_{\text{c}} \\ &\times \left\{ \lim_{\omega \rightarrow k^+} - \lim_{\omega \rightarrow k^-} \right\} \left[\rho_{10110}^{(0,0)} - \rho_{11010}^{(0,0)} - \rho_{11110}^* \right]. \end{aligned} \quad (\text{B1})$$

The first two master integrals above factorise:

$$\begin{aligned} \rho_{10110}^{(0,0)} - \rho_{11010}^{(0,0)} &= \\ \text{Im} \left\{ \left(\not\int_{\text{P}} \frac{1}{P^2(K-P)^2} \right) \left(\not\int_{\text{R}} \frac{1}{R^2} - \not\int_{\text{R}} \frac{1}{Q^2} \right) \right\}, \end{aligned} \quad (\text{B2})$$

¹⁷ The NA60+ Collaboration estimates that chiral symmetry restoration at SPS energies would lead to a difference in the dilepton spectrum of 20-25%, in the window of invariant mass [0.9, 1.4] GeV [89].

where we changed integration variables from Q to $R = K - P - Q$ in the second term. The second factor is real, and proportional to m_∞^2 because

$$\oint_R \frac{1}{R^2} = \frac{T^2}{12}, \quad \oint_Q \frac{1}{Q^2} = -\frac{1}{24} \left(T^2 + 3 \frac{\mu^2}{\pi^2} \right).$$

The first factor is just a one-loop integral (the same is encountered in the LO calculation), it reads

$$\text{Im} \left(\oint_P \frac{1}{P^2(K-P)^2} \right) = \frac{\omega}{k} \langle 1 \rangle$$

which gives a discontinuity

$$\left\{ \rho_{10110}^{(0,0)} - \rho_{11010}^{(0,0)} \right\} \Big|_{\text{disc}} = \frac{(T^2 + \frac{\mu^2}{\pi^2})}{128\pi k} \times \int_{-\infty}^{\infty} d\epsilon \left\{ 1 - f_{\text{F}}(\epsilon - \mu) - f_{\text{F}}(k - \epsilon + \mu) \right\}. \quad (\text{B3})$$

Where the Cauchy principal value of the integral above is implied. As for the last master integral in (B1), it has the following discontinuity:

$$\rho_{11110}^{\star} \Big|_{\text{disc}} = \frac{(T^2 + \frac{\mu^2}{\pi^2})}{256\pi} \int_{-\infty}^{\infty} d\epsilon \left\{ \left[1 - f_{\text{F}}(\epsilon - \mu) - f_{\text{F}}(k - \epsilon + \mu) \right] \left(\frac{1}{\epsilon} + \frac{1}{\omega - \epsilon} \right) \right\}, \quad (\text{B4})$$

which may be obtained after reinstating μ in Eq. (5.15) from Ref. [71].

Altogether, the discontinuity predicted from (B1) turns out to agree with Eq. (28). The transverse LPM spectral function has

$$\rho_{\text{T}} \Big|_{\text{disc}}^{(g^2)} = \frac{N_c m_\infty^2}{8\pi} \int_{-\infty}^{\infty} d\epsilon \left\{ \left[1 - f_{\text{F}}(\epsilon - \mu) - f_{\text{F}}(k - \epsilon + \mu) \right] \left(\frac{2}{k} - \frac{1}{\epsilon} - \frac{1}{k - \epsilon} \right) \right\}. \quad (\text{B5})$$

The $\frac{2}{k}$ -term in parentheses matches with (B3), and the $(\frac{1}{\epsilon} + \frac{1}{k - \epsilon})$ -term matches with (B4). An explicit numerical demonstration that the resummed spectral function is both finite and continuous across the light cone can be found in Fig. (3) of Ref. [39].

Appendix C: Dilepton rapidity distribution

In a simplified system, we illustrate the thermal smearing effect on the rapidity-dependent yields discussed in Sec. IV B. According to Eqs. (35-38), the differential rate from a specific spacetime coordinate is given by

$$\frac{d\Gamma_{\ell\bar{\ell}}}{dM dy} = M \int d^2\mathbf{k}_\perp \left. \frac{d\Gamma_{\ell\bar{\ell}}}{d\omega d^3\mathbf{k}} \right|_{K^\mu = \Lambda^{\mu\nu} K'_\nu}, \quad (\text{C1})$$

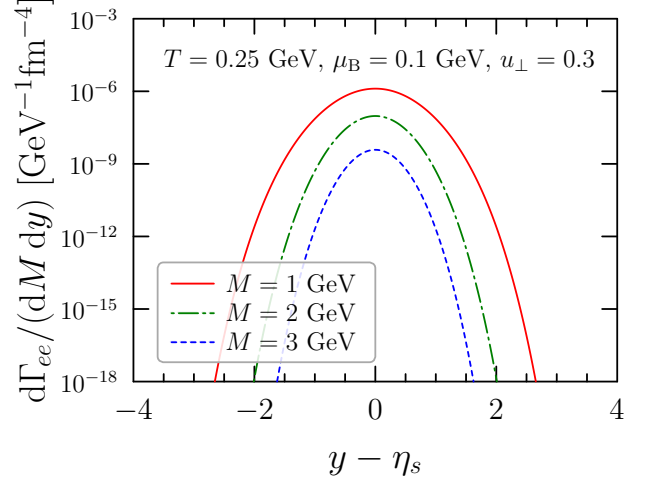


Figure A1. Double differential dilepton rate from Eq. (C1), as a function of $y - \eta_s$, assuming longitudinal boost invariance. The curves are shown for $M = \{1, 2, 3\}$ GeV with $T = 0.25$ GeV and $\mu_B = 0.1$ GeV and $u_\perp = 0.3$.

where K'_μ is measured in the laboratory frame (and thus so are y and \mathbf{k}_\perp , cf. Eq. (37)), while K_μ is the four-momentum in the LRF where the integrand is calculated. For a volume element flowing with a four-velocity $u_\mu(t, \mathbf{x})$, the transformation $\Lambda(t, \mathbf{x})$ from the laboratory frame to the LRF leads to

$$\omega = K'_\mu u^\mu, \quad k = \sqrt{(K'_\mu u^\mu)^2 - M^2}, \quad (\text{C2})$$

for the arguments of the spectral function.

In a boost invariant scenario, with Bjorken expansion (in the z -direction, i.e. $v_z = z/t$), the fluid velocity is assumed to take the form

$$u^\mu = \gamma_\perp (\cosh \eta_s, \mathbf{v}_\perp, \sinh \eta_s), \quad \gamma_\perp \equiv \frac{1}{\sqrt{1 - \mathbf{v}_\perp^2}},$$

where \mathbf{v}_\perp is the transverse flow [93]. Hence the replacement (C2) reads:

$$\omega = \gamma_\perp [M_\perp \cosh(y - \eta_s) - k_\perp v_\perp \cos \varphi], \quad k = \sqrt{\omega^2 - M^2}, \quad (\text{C3})$$

where we used Eq. (37) and introduced φ as the azimuth, taken as the angle between \mathbf{k}_\perp and \mathbf{v}_\perp .

It may be observed that Eq. (C1) is peaked around $y \approx \eta_s$, because the factor $f_{\text{B}}(\omega)$ is largest when ω is minimized. For $M_\perp \gg T$, which is expected to hold for intermediate mass dileptons, a source at spacetime rapidity η_s mostly emits dileptons with the same rapidity in momentum-space.¹⁸ Therefore, when integrating the

¹⁸ To derive this rigorously, one can make use of the identity

$$\lim_{a \rightarrow \infty} (e^{a \cosh x + b} - 1)^{-1} = e^{-(a+b)} \sqrt{2\pi/a} \delta(x).$$

rate over y , like in Eq. (39) for the yield, we only pick up a contribution from spacetime coordinates with $\eta_s \in [y_{\min}, y_{\max}]$. For such cells, the rate is

$$\begin{aligned} \frac{d\Gamma_{\ell\bar{\ell}}}{dM \Delta y} &\simeq \frac{\alpha_{\text{em}}^2}{9\pi^3 M \Delta y} \sqrt{\frac{8T}{\pi^5 \gamma_{\perp}}} \int_{k_{\min}}^{k_{\max}} \frac{dk_{\perp} k_{\perp}}{\sqrt{M_{\perp}}} \int_0^{2\pi} d\varphi \\ &\times \exp\left[-\frac{\omega^*}{T}\right] \rho_V(\omega^*, k^*), \end{aligned} \quad (\text{C4})$$

where ω^* and k^* are given by (C3) with $y = \eta_s$. In the boost invariant setup we are considering, local thermodynamic variables are functions of only \mathbf{x}_{\perp} and τ implying that (C4) is flat w.r.t. η_s .

Exploring the rapidity dependence of the yields is particularly imperative for low beam energy collisions. To

emphasize this, we perform a numerical integration of Eq. (C1) under the assumption of boost invariance and simply set $k_{\min} = 0$ and $k_{\max} = \infty$. Figure A1 shows the rate which is a (symmetric) function of the rapidity difference $y - \eta_s$ because of Eq. (C3). For illustration, we set $T = 0.25$ GeV and $\mu_B = 0.1$ GeV and $u_{\perp} = 0.3$. This demonstrates that indeed the rate is concentrated around $y = \eta_s$ and the width decreases as a function of the invariant mass. Given the finite width, compared to the limit in footnote 18, it's also crucial to compute dilepton production from a (3+1)-dimensional boost-non-invariant system generated in low beam energy collisions. This is necessary for making quantitative comparisons with experimental measurements within a specified rapidity window, instead of taking the 'central value' for y .

-
- [1] See, for example, John W. Harris and Berndt Müller, "QGP Signatures" Revisited," (2023), [arXiv:2308.05743 \[hep-ph\]](#), and references therein.
- [2] Edward V. Shuryak, "Quark-Gluon Plasma and Hadronic Production of Leptons, Photons and Psions," *Phys. Lett. B* **78**, 150 (1978).
- [3] Robert D. Pisarski, "Phenomenology of the Chiral Phase Transition," *Phys. Lett. B* **110**, 155–158 (1982).
- [4] K. Kajantie and H. I. Miettinen, "Temperature Measurement of Quark-Gluon Plasma Formed in High-Energy Nucleus-Nucleus Collisions," *Z. Phys. C* **9**, 341 (1981).
- [5] R. C. Hwa and K. Kajantie, "Diagnosing Quark Matter by Measuring the Total Entropy and the Photon Or Dilepton Emission Rates," *Phys. Rev. D* **32**, 1109 (1985).
- [6] K. Kajantie, Joseph I. Kapusta, Larry D. McLerran, and A. Mekjian, "Dilepton Emission and the QCD Phase Transition in Ultrarelativistic Nuclear Collisions," *Phys. Rev. D* **34**, 2746 (1986).
- [7] See, for example, Charles Gale, "Photon Production in Hot and Dense Strongly Interacting Matter," *Landolt-Bornstein* **23**, 445 (2010), [arXiv:0904.2184 \[hep-ph\]](#), and references therein.
- [8] Ralf Rapp and Hendrik van Hees, "Thermal Dileptons as Fireball Thermometer and Chronometer," *Phys. Lett. B* **753**, 586–590 (2016), [arXiv:1411.4612 \[hep-ph\]](#).
- [9] Jean-François Paquet, "Thermal photon production in Gubser inviscid relativistic fluid dynamics," *Phys. Rev. C* **108**, 064912 (2023), [arXiv:2305.10669 \[nucl-th\]](#).
- [10] Hendrik van Hees, Charles Gale, and Ralf Rapp, "Thermal Photons and Collective Flow at the Relativistic Heavy-Ion Collider," *Phys. Rev. C* **84**, 054906 (2011), [arXiv:1108.2131 \[hep-ph\]](#).
- [11] Chun Shen, Ulrich W. Heinz, Jean-François Paquet, and Charles Gale, "Thermal photons as a quark-gluon plasma thermometer reexamined," *Phys. Rev. C* **89**, 044910 (2014), [arXiv:1308.2440 \[nucl-th\]](#).
- [12] M. Strickland, "Thermal photons and dileptons from nonequilibrium quark - gluon plasma," *Phys. Lett. B* **331**, 245–250 (1994).
- [13] Dinesh K. Srivastava and Klaus Geiger, "Flash of photons from the early stage of heavy ion collisions," *Phys. Rev. C* **58**, 1734–1737 (1998), [arXiv:nucl-th/9802034](#).
- [14] Moritz Greif, Florian Senzel, Heiner Kremer, Kai Zhou, Carsten Greiner, and Zhe Xu, "Nonequilibrium photon production in partonic transport simulations," *Phys. Rev. C* **95**, 054903 (2017), [arXiv:1612.05811 \[hep-ph\]](#).
- [15] Sigtryggur Hauksson, Sangyong Jeon, and Charles Gale, "Photon emission from quark-gluon plasma out of equilibrium," *Phys. Rev. C* **97**, 014901 (2018), [arXiv:1709.03598 \[nucl-th\]](#).
- [16] Jessica Churchill, Li Yan, Sangyong Jeon, and Charles Gale, "Emission of electromagnetic radiation from the early stages of relativistic heavy-ion collisions," *Phys. Rev. C* **103**, 024904 (2021), [arXiv:2008.02902 \[hep-ph\]](#).
- [17] Charles Gale, Jean-François Paquet, Björn Schenke, and Chun Shen, "Multimessenger heavy-ion collision physics," *Phys. Rev. C* **105**, 014909 (2022), [arXiv:2106.11216 \[nucl-th\]](#).
- [18] Maurice Coquet, Xiaojian Du, Jean-Yves Ollitrault, Soeren Schlichting, and Michael Winn, "Intermediate mass dileptons as pre-equilibrium probes in heavy ion collisions," *Phys. Lett. B* **821**, 136626 (2021), [arXiv:2104.07622 \[nucl-th\]](#).
- [19] Charles Gale and Joseph I. Kapusta, "Dilepton radiation from high temperature nuclear matter," *Phys. Rev. C* **35**, 2107–2116 (1987).
- [20] Charles Gale and Peter Lichard, "Lepton pairs from thermal mesons," *Phys. Rev. D* **49**, 3338–3344 (1994), [arXiv:hep-ph/9307363](#).
- [21] K. Geiger and Joseph I. Kapusta, "Dilepton radiation from cascading partons in ultrarelativistic nuclear collisions," *Phys. Rev. Lett.* **70**, 1920–1923 (1993).
- [22] Burkhard Kampfer, O. P. Pavlenko, A. Peshier, and G. Soff, "Dilepton production in a chemically equilibrating, expanding, and hadronizing quark - gluon plasma," *Phys. Rev. C* **52**, 2704–2713 (1995).
- [23] P. Huovinen, M. Belkacem, P. J. Ellis, and Joseph I. Kapusta, "Dileptons and photons from coarse grained microscopic dynamics and hydrodynamics compared to experimental data," *Phys. Rev. C* **66**, 014903 (2002), [arXiv:nucl-th/0203023](#).
- [24] Ralf Rapp, "Dilepton Spectroscopy of QCD Matter

- at Collider Energies,” *Adv. High Energy Phys.* **2013**, 148253 (2013), [arXiv:1304.2309 \[hep-ph\]](#).
- [25] Gojko Vujanovic, Clint Young, Bjoern Schenke, Ralf Rapp, Sangyong Jeon, and Charles Gale, “Dilepton emission in high-energy heavy-ion collisions with viscous hydrodynamics,” *Phys. Rev. C* **89**, 034904 (2014), [arXiv:1312.0676 \[nucl-th\]](#).
- [26] Gojko Vujanovic, Jean-François Paquet, Gabriel S. Denicol, Matthew Luzum, Sangyong Jeon, and Charles Gale, “Electromagnetic radiation as a probe of the initial state and of viscous dynamics in relativistic nuclear collisions,” *Phys. Rev. C* **94**, 014904 (2016), [arXiv:1602.01455 \[nucl-th\]](#).
- [27] Gojko Vujanovic, Jean-François Paquet, Chun Shen, Gabriel S. Denicol, Sangyong Jeon, Charles Gale, and Ulrich Heinz, “Exploring the influence of bulk viscosity of QCD on dilepton tomography,” *Phys. Rev. C* **101**, 044904 (2020), [arXiv:1903.05078 \[nucl-th\]](#).
- [28] Oleh Savchuk, Anton Motornenko, Jan Steinheimer, Volodymyr Vovchenko, Marcus Bleicher, Mark Gorenstein, and Tetyana Galatyuk, “Enhanced dilepton emission from a phase transition in dense matter,” *J. Phys. G* **50**, 125104 (2023), [arXiv:2209.05267 \[nucl-th\]](#).
- [29] Gianluca Usai *et al.* (NA60+), “Study of hard and electromagnetic processes at CERN-SPS energies: an investigation of the high- μ_B region of the QCD phase diagram with NA60+,” *JPS Conf. Proc.* **33**, 011113 (2021), [arXiv:1812.07948 \[nucl-ex\]](#).
- [30] Enrico Scomparin (NA60+), “Measuring Dilepton and Heavy-quark Production at Large μ_B : The NA60+ Experiment at the CERN SPS,” *Acta Phys. Polon. Supp.* **16**, 1–A144 (2023), [arXiv:2209.06778 \[nucl-ex\]](#).
- [31] Charles Gale, Yoshimasa Hidaka, Sangyong Jeon, Shu Lin, Jean-François Paquet, Robert D. Pisarski, Daisuke Satow, Vladimir V. Skokov, and Gojko Vujanovic, “Production and Elliptic Flow of Dileptons and Photons in a Matrix Model of the Quark-Gluon Plasma,” *Phys. Rev. Lett.* **114**, 072301 (2015), [arXiv:1409.4778 \[hep-ph\]](#).
- [32] Hualong Gervais and Sangyong Jeon, “Photon Production from a Quark-Gluon-Plasma at Finite Baryon Chemical Potential,” *Phys. Rev. C* **86**, 034904 (2012), [arXiv:1206.6086 \[nucl-th\]](#).
- [33] I. Ghisoiu and M. Laine, “Interpolation of hard and soft dilepton rates,” *JHEP* **10**, 083 (2014), [arXiv:1407.7955 \[hep-ph\]](#).
- [34] H. A. Weldon, “Reformulation of finite temperature dilepton production,” *Phys. Rev. D* **42**, 2384–2387 (1990).
- [35] Charles Gale and Joseph I. Kapusta, “Vector dominance model at finite temperature,” *Nucl. Phys. B* **357**, 65–89 (1991).
- [36] D. Bödeker, M. Sangel, and M. Wörmann, “Equilibration, particle production, and self-energy,” *Phys. Rev. D* **93**, 045028 (2016), [arXiv:1510.06742 \[hep-ph\]](#).
- [37] Jean-Paul Blaizot and Francois Gelis, “Photon and dilepton production in the quark-gluon plasma: Perturbation theory vs lattice QCD,” *Eur. Phys. J. C* **43**, 375–380 (2005), [arXiv:hep-ph/0504144](#).
- [38] G. Jackson and M. Laine, “Testing thermal photon and dilepton rates,” *JHEP* **11**, 144 (2019), [arXiv:1910.09567 \[hep-ph\]](#).
- [39] Greg Jackson, “Shedding light on thermal photon and dilepton production,” *EPJ Web Conf.* **274**, 05014 (2022), [arXiv:2211.09575 \[hep-ph\]](#).
- [40] Dibyendu Bala, Sajid Ali, Anthony Francis, Greg Jackson, Olaf Kaczmarek, and Tristan Ueding, “Photon production rate from Transverse-Longitudinal (T–L) mesonic correlator on the lattice,” *PoS LATTICE2022*, 169 (2023), [arXiv:2212.11509 \[hep-lat\]](#).
- [41] R. Baier, B. Pire, and D. Schiff, “Dilepton production at finite temperature: Perturbative treatment at order α_s ,” *Phys. Rev. D* **38**, 2814 (1988).
- [42] Y. Gabellini, T. Grandou, and D. Poizat, “Electron - Positron Annihilation in Thermal QCD,” *Annals Phys.* **202**, 436–466 (1990).
- [43] T. Altherr and P. Aurenche, “Finite Temperature QCD Corrections to Lepton Pair Formation in a Quark - Gluon Plasma,” *Z. Phys. C* **45**, 99 (1989).
- [44] Eric Braaten and Robert D. Pisarski, “Soft Amplitudes in Hot Gauge Theories: A General Analysis,” *Nucl. Phys. B* **337**, 569–634 (1990).
- [45] Eric Braaten, Robert D. Pisarski, and Tzu-Chiang Yuan, “Production of Soft Dileptons in the Quark - Gluon Plasma,” *Phys. Rev. Lett.* **64**, 2242 (1990).
- [46] Guy D. Moore and Jean-Marie Robert, “Dileptons, spectral weights, and conductivity in the quark-gluon plasma,” (2006), [arXiv:hep-ph/0607172](#).
- [47] Joseph I. Kapusta, P. Lichard, and D. Seibert, “High-energy photons from quark - gluon plasma versus hot hadronic gas,” *Phys. Rev. D* **44**, 2774–2788 (1991), [Erratum: *Phys.Rev.D* 47, 4171 (1993)].
- [48] R. Baier, H. Nakkagawa, A. Niegawa, and K. Redlich, “Production rate of hard thermal photons and screening of quark mass singularity,” *Z. Phys. C* **53**, 433–438 (1992).
- [49] Harvey B. Meyer, Marco Cè, Tim Harris, Arianna Toniato, and Csaba Török, “Deep inelastic scattering off quark-gluon plasma and its photon emissivity,” *PoS LATTICE2021*, 269 (2022), [arXiv:2112.00450 \[hep-lat\]](#).
- [50] P. Aurenche, F. Gelis, G. D. Moore, and H. Zaraket, “Landau-Pomeranchuk-Migdal resummation for dilepton production,” *JHEP* **12**, 006 (2002), [arXiv:hep-ph/0211036](#).
- [51] P. Aurenche, F. Gelis, and H. Zaraket, “Enhanced thermal production of hard dileptons by $3 \rightarrow 2$ processes,” *JHEP* **07**, 063 (2002), [arXiv:hep-ph/0204145](#).
- [52] Jacopo Ghiglieri, Juhee Hong, Alekski Kurkela, Egang Lu, Guy D. Moore, and Derek Teaney, “Next-to-leading order thermal photon production in a weakly coupled quark-gluon plasma,” *JHEP* **05**, 010 (2013), [arXiv:1302.5970 \[hep-ph\]](#).
- [53] Jacopo Ghiglieri and Guy D. Moore, “Low Mass Thermal Dilepton Production at NLO in a Weakly Coupled Quark-Gluon Plasma,” *JHEP* **12**, 029 (2014), [arXiv:1410.4203 \[hep-ph\]](#).
- [54] Peter Brockway Arnold, Guy D. Moore, and Laurence G. Yaffe, “Photon emission from ultrarelativistic plasmas,” *JHEP* **11**, 057 (2001), [arXiv:hep-ph/0109064](#).
- [55] Peter Brockway Arnold, Guy D. Moore, and Laurence G. Yaffe, “Photon emission from quark gluon plasma: Complete leading order results,” *JHEP* **12**, 009 (2001), [arXiv:hep-ph/0111107](#).
- [56] S. Caron-Huot, “Asymptotics of thermal spectral functions,” *Phys. Rev. D* **79**, 125009 (2009), [arXiv:0903.3958 \[hep-ph\]](#).
- [57] Chun Shen and Sahr Alzhrani, “Collision-geometry-based 3D initial condition for relativistic heavy-ion collisions,” *Phys. Rev. C* **102**, 014909 (2020), [arXiv:2003.05852](#)

- [nucl-th].
- [58] “iEBE-MUSIC, a fully integrated numerical framework to automate hybrid simulations for relativistic heavy-ion collisions.” <https://github.com/LipeiDu/iEBE-MUSIC>.
- [59] Gabriel S. Denicol, Charles Gale, Sangyong Jeon, Akihiko Monnai, Björn Schenke, and Chun Shen, “Net baryon diffusion in fluid dynamic simulations of relativistic heavy-ion collisions,” *Phys. Rev. C* **98**, 034916 (2018), [arXiv:1804.10557 \[nucl-th\]](https://arxiv.org/abs/1804.10557).
- [60] Lipei Du and Ulrich Heinz, “(3+1)-dimensional dissipative relativistic fluid dynamics at non-zero net baryon density,” *Comput. Phys. Commun.* **251**, 107090 (2020), [arXiv:1906.11181 \[nucl-th\]](https://arxiv.org/abs/1906.11181).
- [61] G. S. Denicol, H. Niemi, E. Molnar, and D. H. Rischke, “Derivation of transient relativistic fluid dynamics from the Boltzmann equation,” *Phys. Rev. D* **85**, 114047 (2012), [Erratum: *Phys.Rev.D* 91, 039902 (2015)], [arXiv:1202.4551 \[nucl-th\]](https://arxiv.org/abs/1202.4551).
- [62] Lipei Du, Han Gao, Sangyong Jeon, and Charles Gale, “Rapidity scan with multistage hydrodynamic and statistical thermal models,” *Phys. Rev. C* **109**, 014907 (2024), [arXiv:2302.13852 \[nucl-th\]](https://arxiv.org/abs/2302.13852).
- [63] Bjoern Schenke, Sangyong Jeon, and Charles Gale, “(3+1)D hydrodynamic simulation of relativistic heavy-ion collisions,” *Phys. Rev. C* **82**, 014903 (2010), [arXiv:1004.1408 \[hep-ph\]](https://arxiv.org/abs/1004.1408).
- [64] Bjorn Schenke, Sangyong Jeon, and Charles Gale, “Elliptic and triangular flow in event-by-event (3+1)D viscous hydrodynamics,” *Phys. Rev. Lett.* **106**, 042301 (2011), [arXiv:1009.3244 \[hep-ph\]](https://arxiv.org/abs/1009.3244).
- [65] Akihiko Monnai, Björn Schenke, and Chun Shen, “Equation of state at finite densities for QCD matter in nuclear collisions,” *Phys. Rev. C* **100**, 024907 (2019), [arXiv:1902.05095 \[nucl-th\]](https://arxiv.org/abs/1902.05095).
- [66] J. Cleymans, H. Oeschler, K. Redlich, and S. Wheaton, “Comparison of chemical freeze-out criteria in heavy-ion collisions,” *Phys. Rev. C* **73**, 034905 (2006), [arXiv:hep-ph/0511094](https://arxiv.org/abs/hep-ph/0511094).
- [67] S. A. Bass *et al.*, “Microscopic models for ultrarelativistic heavy ion collisions,” *Prog. Part. Nucl. Phys.* **41**, 255–369 (1998), [arXiv:nucl-th/9803035](https://arxiv.org/abs/nucl-th/9803035).
- [68] M. Bleicher *et al.*, “Relativistic hadron hadron collisions in the ultrarelativistic quantum molecular dynamics model,” *J. Phys. G* **25**, 1859–1896 (1999), [arXiv:hep-ph/9909407](https://arxiv.org/abs/hep-ph/9909407).
- [69] A. Dumitru, D. H. Rischke, T. Schönfeld, L. Winkelmann, Horst Stöcker, and W. Greiner, “Suppression of dilepton production at finite baryon density,” *Phys. Rev. Lett.* **70**, 2860–2863 (1993).
- [70] M. Laine, “Thermal 2-loop master spectral function at finite momentum,” *JHEP* **05**, 083 (2013), [arXiv:1304.0202 \[hep-ph\]](https://arxiv.org/abs/1304.0202).
- [71] G. Jackson, “Two-loop thermal spectral functions with general kinematics,” *Phys. Rev. D* **100**, 116019 (2019), [arXiv:1910.07552 \[hep-ph\]](https://arxiv.org/abs/1910.07552).
- [72] M. Laine, “NLO thermal dilepton rate at non-zero momentum,” *JHEP* **11**, 120 (2013), [arXiv:1310.0164 \[hep-ph\]](https://arxiv.org/abs/1310.0164).
- [73] Christoph T. Traxler, Hans Vija, and Markus H. Thoma, “Hard photon production rate of a quark - gluon plasma at finite quark chemical potential,” *Phys. Lett. B* **346**, 329–334 (1995), [arXiv:hep-ph/9410309](https://arxiv.org/abs/hep-ph/9410309).
- [74] P. Aurenche, F. Gelis, and H. Zaraket, “A Simple sum rule for the thermal gluon spectral function and applications,” *JHEP* **05**, 043 (2002), [arXiv:hep-ph/0204146](https://arxiv.org/abs/hep-ph/0204146).
- [75] J. Ghiglieri and M. Laine, “Smooth interpolation between thermal Born and LPM rates,” *JHEP* **01**, 173 (2022), [arXiv:2110.07149 \[hep-ph\]](https://arxiv.org/abs/2110.07149).
- [76] “DileptonEmission, a dilepton code designed to compute dilepton distributions with next-to-leading-order (NLO) emission rates at non-zero chemical potentials, integrated over a hydrodynamic spacetime evolution.” <https://github.com/LipeiDu/DileptonEmission>.
- [77] M. Arslanok *et al.*, “Hot QCD White Paper,” (2023), [arXiv:2303.17254 \[nucl-ex\]](https://arxiv.org/abs/2303.17254).
- [78] Radoslaw Ryblewski and Michael Strickland, “Dilepton production from the quark-gluon plasma using (3+1)-dimensional anisotropic dissipative hydrodynamics,” *Phys. Rev. D* **92**, 025026 (2015), [arXiv:1501.03418 \[nucl-th\]](https://arxiv.org/abs/1501.03418).
- [79] Yannis Burnier and Chiara Gastaldi, “Contribution of next-to-leading order and Landau-Pomeranchuk-Migdal corrections to thermal dilepton emission in heavy-ion collisions,” *Phys. Rev. C* **93**, 044902 (2016), [arXiv:1508.06978 \[nucl-th\]](https://arxiv.org/abs/1508.06978).
- [80] L. Adamczyk *et al.* (STAR), “Bulk Properties of the Medium Produced in Relativistic Heavy-Ion Collisions from the Beam Energy Scan Program,” *Phys. Rev. C* **96**, 044904 (2017), [arXiv:1701.07065 \[nucl-ex\]](https://arxiv.org/abs/1701.07065).
- [81] Lipei Du, Chun Shen, Sangyong Jeon, and Charles Gale, “Probing initial baryon stopping and equation of state with rapidity-dependent directed flow of identified particles,” *Phys. Rev. C* **108**, L041901 (2023), [arXiv:2211.16408 \[nucl-th\]](https://arxiv.org/abs/2211.16408).
- [82] J. Adamczewski-Musch *et al.* (HADES), “Probing dense baryon-rich matter with virtual photons,” *Nature Phys.* **15**, 1040–1045 (2019).
- [83] R. Rapp, J. Wambach, and H. van Hees, “The Chiral Restoration Transition of QCD and Low Mass Dileptons,” *Landolt-Bornstein* **23**, 134 (2010), [arXiv:0901.3289 \[hep-ph\]](https://arxiv.org/abs/0901.3289).
- [84] L. Adamczyk *et al.* (STAR), “Dielectron Mass Spectra from Au+Au Collisions at $\sqrt{s_{NN}} = 200$ GeV,” *Phys. Rev. Lett.* **113**, 022301 (2014), [Addendum: *Phys.Rev.Lett.* 113, 049903 (2014)], [arXiv:1312.7397 \[hep-ex\]](https://arxiv.org/abs/1312.7397).
- [85] L. Adamczyk *et al.* (STAR), “Measurements of Dielectron Production in Au+Au Collisions at $\sqrt{s_{NN}} = 200$ GeV from the STAR Experiment,” *Phys. Rev. C* **92**, 024912 (2015), [arXiv:1504.01317 \[hep-ex\]](https://arxiv.org/abs/1504.01317).
- [86] L. Adamczyk *et al.* (STAR), “Energy dependence of acceptance-corrected dielectron excess mass spectrum at mid-rapidity in Au+Au collisions at $\sqrt{s_{NN}} = 19.6$ and 200 GeV,” *Phys. Lett. B* **750**, 64–71 (2015), [arXiv:1501.05341 \[hep-ex\]](https://arxiv.org/abs/1501.05341).
- [87] M. I. Abdulhamid *et al.* (STAR), “Measurements of dielectron production in Au+Au collisions at $s_{NN}=27, 39$, and 62.4 GeV from the STAR experiment,” *Phys. Rev. C* **107**, L061901 (2023).
- [88] Jessica Churchill, Lipei Du, Charles Gale, Greg Jackson, and Sangyong Jeon, “Virtual Photons Shed Light on the Early Temperature of Dense QCD Matter,” (2023), [arXiv:2311.06951 \[nucl-th\]](https://arxiv.org/abs/2311.06951).
- [89] C. Ahdida, G. Alocco, F. Antinori, M. Arba, M. Aresti, R. Arnaldi, A. Baratto Roldan, S. Beole, A. Beraudo, J. Bernhard, L. Bianchi, *et al.* (NA60+), “Letter of Intent: the NA60+ experiment,” (2022), [arXiv:2212.14452 \[nucl-ex\]](https://arxiv.org/abs/2212.14452).
- [90] Paul M. Hohler and Ralf Rapp, “Is ρ -Meson Melting

- Compatible with Chiral Restoration?" *Phys. Lett. B* **731**, 103–109 (2014), [arXiv:1311.2921 \[hep-ph\]](#).
- [91] G. Jackson and M. Laine, "Efficient numerical integration of thermal interaction rates," *JHEP* **09**, 125 (2021), [arXiv:2107.07132 \[hep-ph\]](#).
- [92] G. Jackson, 2023, (Online). <http://doi.org/10.5281/zenodo.3478143>.
- [93] J. D. Bjorken, "Highly Relativistic Nucleus-Nucleus Collisions: The Central Rapidity Region," *Phys. Rev. D* **27**, 140–151 (1983).